

A case report of clonal EBV-like memory CD4⁺ T cell activation in fatal checkpoint inhibitor-induced encephalitis

Douglas B. Johnson^{1,2,22*}, Wyatt J. McDonnell^{1,2,3,4,5,22}, Paula I. Gonzalez-Ericsson^{1,6}, Rami N. Al-Rohil^{3,7}, Bret C. Mobley³, Joe-Elie Salem^{1,8}, Daniel Y. Wang¹, Violeta Sanchez³, Yu Wang^{1,9}, Cody A. Chastain¹, Kristi Barker¹⁰, Yan Liang¹⁰, Sarah Warren¹⁰, Joseph M. Beechem¹⁰, Alexander M. Menzies^{11,12,13,14}, Martin Tio¹¹, Georgina V. Long^{11,12,13,14}, Justine V. Cohen¹⁵, Amanda C. Guidon¹⁵, Méabh O'Hare¹⁵, Sunandana Chandra¹⁶, Akansha Chowdhary¹⁶, Bénédicte Lebrun-Vignes⁸, Simone M. Goldinger¹⁷, Elisabeth J. Rushing¹⁸, Elizabeth I. Buchbinder¹⁹, Simon A. Mallal^{1,2,3,4,20}, Chanjuan Shi³, Yaomin Xu^{1,9}, Javid J. Moslehi¹, Melinda E. Sanders³, Jeffrey A. Sosman²¹ and Justin M. Balko^{1,2,3,6*}

Checkpoint inhibitors produce durable responses in numerous metastatic cancers, but immune-related adverse events (irAEs) complicate and limit their benefit. IrAEs can affect organ systems idiosyncratically; presentations range from mild and self-limited to fulminant and fatal. The molecular mechanisms underlying irAEs are poorly understood. Here, we report a fatal case of encephalitis arising during anti-programmed cell death receptor 1 therapy in a patient with metastatic melanoma. Histologic analyses revealed robust T cell infiltration and prominent programmed death ligand 1 expression. We identified 209 reported cases in global pharmacovigilance databases (across multiple cancer types) of encephalitis associated with checkpoint inhibitor regimens, with a 19% fatality rate. We performed further analyses from the index case and two additional cases to shed light on this recurrent and fulminant irAE. Spatial and multi-omic analyses pinpointed activated memory CD4⁺ T cells as highly enriched in the inflamed, affected region. We identified a highly oligoclonal T cell receptor repertoire, which we localized to activated memory cytotoxic (CD45RO⁺GZMB⁺Ki67⁺) CD4 cells. We also identified Epstein-Barr virus-specific T cell receptors and EBV⁺ lymphocytes in the affected region, which we speculate contributed to neural inflammation in the index case. Collectively, the three cases studied here identify CD4⁺

and CD8⁺ T cells as culprits of checkpoint inhibitor-associated immune encephalitis.

Monoclonal antibodies blocking key negative regulators of T cell function have transformed the management of numerous cancers¹. While immune checkpoint inhibitors (ICIs) induce durable responses in some patients, aberrant immune-mediated phenomena, termed irAEs, may be unleashed in an unpredictable fashion². Most irAEs are self-limited or resolve with glucocorticoids³, although highly morbid and even fatal events can occur^{4–6}. Inflamed tissues affected by irAEs are characterized by robust infiltration by T lymphocytes and myeloid-lineage cells^{5–8}. Uncommon irAEs affecting the central nervous system (such as encephalitis), peripheral nervous system (such as Guillain–Barre and peripheral sensory neuropathy) and neuromuscular junction (such as myasthenia gravis) have been described⁹. The molecular basis of irAEs, including neurologic irAEs, remains poorly understood despite these early findings.

We performed deep molecular profiling of a case of fulminant anti-programmed cell death receptor 1 (PD-1)-induced encephalitis to provide insight into this severe neurologic irAE. We show that ICI-induced encephalitis occurs across cancer settings and is serious or fatal in many patients. Multi-omic analyses of the index case revealed a clonal CD4⁺ activated memory cytotoxic T cell population and robust central nervous system (CNS) infiltration by cytotoxic CD4⁺ and CD8⁺ T cells.

¹Department of Medicine, Vanderbilt University Medical Center, Nashville, TN, USA. ²Vanderbilt Institute for Infection, Immunology and Inflammation, Vanderbilt University Medical Center, Nashville, TN, USA. ³Department of Pathology, Microbiology, and Immunology, Vanderbilt University Medical Center, Nashville, TN, USA. ⁴Center for Translational Immunology and Infectious Disease, Vanderbilt University Medical Center, Nashville, TN, USA. ⁵Vanderbilt Vaccine Center, Vanderbilt University Medical Center, Nashville, TN, USA. ⁶Breast Cancer Research Program, Vanderbilt University Medical Center, Nashville, TN, USA. ⁷Department of Pathology and Dermatology, Duke University Medical Center, Durham, NC, USA. ⁸Sorbonne Université, INSERM CIC Paris-Est, AP-HP, ICAN, Regional Pharmacovigilance Centre, Pitié-Salpêtrière Hospital, Department of Pharmacology, Paris, France. ⁹Department of Biostatistics, Vanderbilt University Medical Center, Nashville, TN, USA. ¹⁰NanoString Technologies, Seattle, WA, USA. ¹¹Melanoma Institute Australia, Sydney, Australia. ¹²The University of Sydney, Sydney, New South Wales, Australia. ¹³Royal North Shore Hospital, Sydney, New South Wales, Australia. ¹⁴Mater Hospital, Sydney, New South Wales, Australia. ¹⁵Massachusetts General Hospital, Boston, MA, USA. ¹⁶Feinberg School of Medicine, Northwestern University, Evanston, IL, USA. ¹⁷Department of Dermatology, University Hospital, Zurich, Switzerland. ¹⁸Institute of Neuropathology, University Hospital, Zurich, Switzerland. ¹⁹Department of Medical Oncology, Dana-Farber Cancer Institute, Boston, MA, USA. ²⁰Institute for Immunology and Infectious Diseases, Perth, Australia. ²¹Northwestern Feinberg School of Medicine, Chicago, IL, USA. ²²These authors contributed equally: Douglas B. Johnson, Wyatt J. McDonnell. *e-mail: douglas.b.johnson@vumc.org; justin.balko@vumc.org

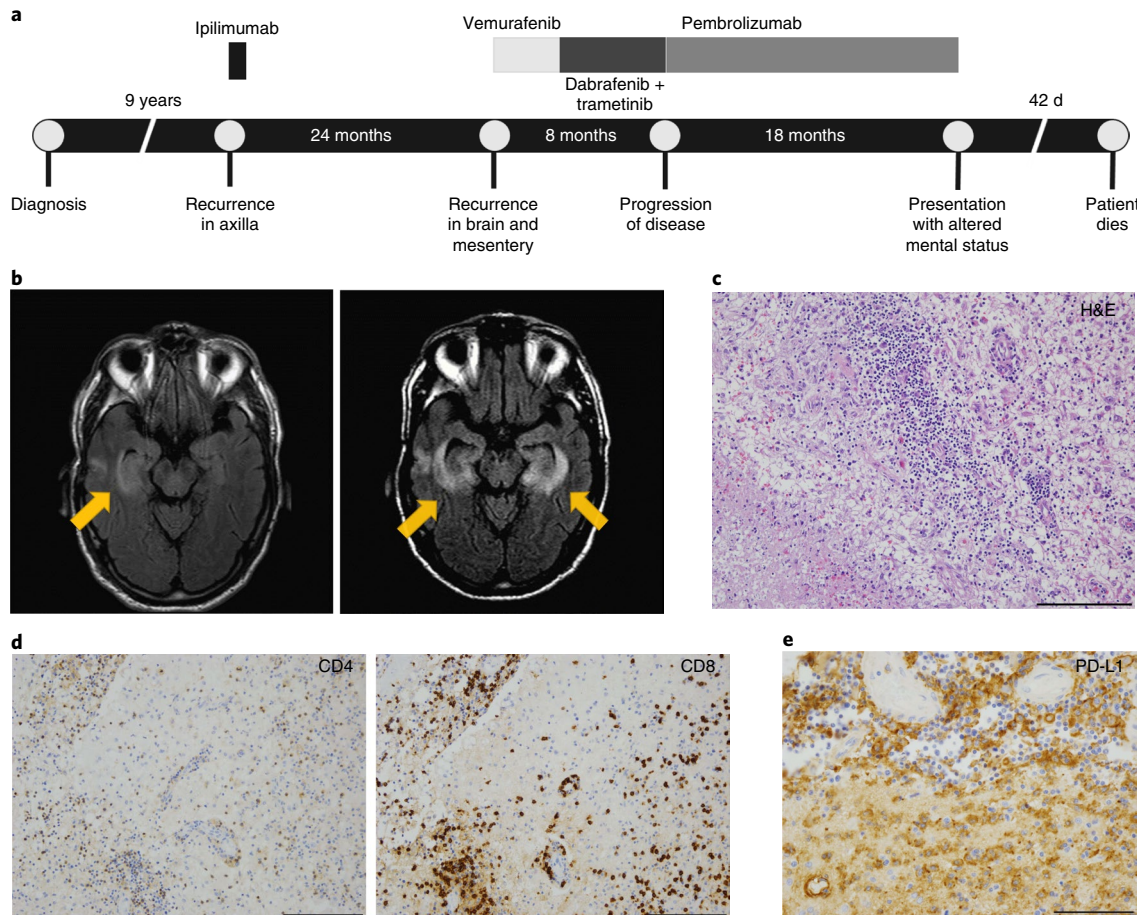


Fig. 1 | Clinical course of anti-PD-1-induced encephalitis and histologic findings at autopsy. **a**, Timeline of index patient diagnosis, prior therapies and anti-PD-1 therapy. **b**, Left: MRI demonstrating restricted diffusion and hyper-intensity in the right temporal lobe and left basal ganglia from the day of hospital admission. Right: MRI showing progressive bilateral medial temporal encephalitis with bilateral putamen involvement. Imaging was performed once at admission and once after admission. **c**, H&E stain shows intense perivascular lymphocytic infiltrate extending to adjacent brain parenchyma, next to a region of infarction (lower left); magnification $\times 20$. **d**, CD4 and CD8 IHC showing the lymphocytic infiltrate is composed of approximately equal ratios of CD4 $^{+}$ and CD8 $^{+}$ T cells; $\times 20$. **e**, Diffuse PD-L1 positivity staining in cells with macrophage morphology surrounding the region of infarction; $\times 20$. Of particular note, tissues collected and assayed in this study anteceded treatment with steroids and anti-tumor necrosis factor α , which could impact the immunologic status of the patient. Slide staining for each marker was performed 1–3 times in parallel with and compared with positive controls for each marker.

A man in his 70s with metastatic melanoma developed meningoencephalitis while receiving pembrolizumab. His prior history was notable for treatment with ipilimumab (complicated by colitis requiring infliximab), brain metastasis treated with resection, and radiation and BRAF and MEK inhibitor therapy (Fig. 1a). Following progression, he received pembrolizumab, resulting in a near-complete response without toxicity. Approximately 18 months into pembrolizumab therapy, he developed nausea, fevers, confusion and aphasia progressing over 2 d. Brain magnetic resonance imaging (MRI) showed restricted diffusion and enhancement in the basal ganglia and right temporal lobe consistent with inflammatory or herpes simplex virus (HSV) encephalitis (Fig. 1b; Supplementary Table 1). Of note, Epstein–Barr virus (EBV) polymerase chain reaction later returned positive with viral load of 1,200 copies ml $^{-1}$ and was persistently detected in the blood (1,888–4,321 copies) and across multiple cerebrospinal fluid (CSF) samples; HSV testing was negative. He continued to have neurologic deterioration requiring intubation and mechanical ventilation; MRI showed progressive encephalitis involving both temporal lobes (Fig. 1b). Methylprednisolone 1 mg kg $^{-1}$ twice daily was initiated 5 d into the hospitalization, leading to dramatic and rapid clinical improvement.

Two weeks later, he developed recurrent neurologic symptoms while tapering steroids; MRI showed worsening of encephalitis. Subsequent CSF evaluation showed evolution to a lymphocytic predominance (83 nucleated cells, 8% neutrophils, 91% lymphocytes). He then had brief episodes of clinical improvement with high-dose steroids and intravenous immunoglobulin, followed by progressive deterioration of his mental status and motor strength. He died 42 d after symptom onset.

To assess the frequency of encephalitis among patients treated with ICIs, we queried VigiBase (see Methods). We identified 209 reports of encephalitis; the median age was 61 years (range 7–85) and 59% had either melanoma or lung cancer (Table 1). Overall, 66% of patients received anti-PD-1 monotherapy; 88% of patients had no other concurrent irAEs reported. The median time to symptom onset was 67 d (range 5–456) and 39 patients (19%) died. In contrast with other toxicities (for example myocarditis)⁴, the fatality rate was similar between encephalitis from anti-PD-1 monotherapy versus combined anti-PD-1 and anti-CTLA-4 therapy (20% versus 26%, $\chi^2 P=0.50$). We next queried 2,501 patients treated with ICIs from four large academic centers to confirm these findings in clinically diagnosed cases of encephalitis and identified 22 cases of meningoencephalitis. These findings (Supplementary Table 2) were

Table 1 | Characteristics of patients with immune checkpoint inhibitor-associated encephalitis (*n*=209)

Characteristic	Number (%)
Male	113 (54)
Female	69 (33)
Not listed	27 (13)
Age (years; median, range)	61, 16–85
Cancer	
Melanoma	44 (21)
Lung cancer (NSCLC and other)	80 (38)
Hodgkin's lymphoma	14 (7)
Non-Hodgkin's lymphoma	3 (1.5)
Renal	9 (4.5)
Other/not listed	59 (28)
Region reporting	
Americas	117 (56)
Europe	67 (32)
Asia	19 (9)
Oceania	6 (3)
Regimen	
Anti-PD-1 monotherapy	137 (66)
Combination anti-PD-1 ^a anti-CTLA-4	31 (15)
Other combinations ^a	14 (7)
Anti-PD-L1 monotherapy	15 (7)
Anti-CTLA-4 (ipilimumab) monotherapy	12 (6)
Timing (d: median, range)	67 (5–456)
Reporting term	
Encephalitis	145 (69)
Encephalitis autoimmune	36 (17)
Limbic encephalitis	15 (7)
Meningoencephalitis	12 (6)
Cerebellitis	1 (1)
Concurrent irAEs	
Colitis	4 (2)
Pneumonitis	6 (3)
Thyroiditis	7 (3)
Myocarditis	2 (1)
Vasculitis	2 (1)
Adrenal insufficiency	4 (2)
Dermatitis	4 (2)
Other ^b	7 (3)
Fatal outcome	39 (19)
Reporting year	
2012–2014	5 (2.5)
2015	5 (2.5)
2016	36 (17)
2017	77 (37)
2018 (to 5 September)	86 (41)

^aAtezolizumab, chemotherapy (*n*=2); atezolizumab, bevacizumab (*n*=2); atezolizumab, cobimetinib (*n*=1); ipilimumab, crizotinib, nivolumab (*n*=1); ipilimumab, bevacizumab (*n*=1); ipilimumab, nivolumab, golutumab (*n*=1); ipilimumab, interferon (*n*=1); ipilimumab, nivolumab, cabozantinib (*n*=1); ipilimumab, aldesleukin (*n*=1); nivolumab, cabozantinib (*n*=1); nivolumab, denosumab (*n*=1); nivolumab, brentuximab (*n*=1); pembrolizumab, chemotherapy (*n*=1).

^bPancreatitis (*n*=1), insulin-dependent type 1 diabetes, hypopituitarism (*n*=2), hypophysitis (*n*=2), cytokine storm (*n*=1), autoimmune nephritis (*n*=1) We used the following MedDRA 21.0 search terms levels for our reaction criteria: encephalitis and/or encephalitis autoimmune and/or limbic encephalitis and/or meningoencephalitis and/or cerebellitis. For our substance criteria, we used pembrolizumab, atezolizumab, nivolumab, durvalumab, avelumab, ipilimumab, tremelimumab and all combinations thereof. NSCLC, non-small cell lung cancer.

similar to the pharmacovigilance database, with a median onset of 80 d (range 4–684). The most frequent presenting symptom was confusion (50%), followed by headaches (36%), seizures (23%) and fevers (18%). Temporal or occipital lobe enhancement was the most common imaging finding (22%, *n*=5). Most patients recovered completely (68%) although five (22%) had persistent neurologic symptoms and two (9%) died; median hospitalization time was 6.5 d (range 2–120). Thus, encephalitis is a rare but recurrent and potentially fatal toxicity of ICIs that occurs across cancer types.

An autopsy of the index case was performed. No evidence of melanoma was observed in the CNS or elsewhere using pan-melanoma stains S100, SOX10, melanoma antigen recognized by T cells 1 (MelanA/MART-1) and MITF (data not shown). Analysis of T cell receptors (reported subsequently in this letter) also did not identify any known or likely MelanA/MART-1-specific HLA-A*02:01-restricted T cell receptors (TCRs). Vigorous inflammation, multiple cerebral infarctions with necrosis and sporadic hemorrhagic transformation were noted in the bilateral temporal lobes and striatum with surrounding gliosis and numerous macrophages (Fig. 1c, Extended Data Fig. 1a). Exuberant perivascular inflammation extending to adjacent gray matter characterized by approximately equal ratios of CD4⁺ and CD8⁺ T cells was observed (Fig. 1d), although we noted that CD4⁺ cells were present in localized patterns while CD8⁺ cells were diffuse and consistently present. We also observed frequent CD68⁺ cells, a macrophage marker which also stains microglial cells (Extended Data Fig. 1b). Minimal CD20⁺ infiltrates or immunoglobulin deposition were observed, suggesting that B cells did not constitute a major component of the inflammatory process (Extended Data Fig. 1c). We observed similar patterns of T cell and macrophage infiltration in inflamed meninges and adjacent gray matter, including perivascular spaces (Extended Data Fig. 2). In contrast, brain tissue obtained from radiographically normal brain was histologically unremarkable with no inflammatory infiltrate (Extended Data Fig. 3).

We then profiled the T cell exhaustion markers PD-1 and programmed death ligand 1 (PD-L1). PD-L1 was diffusely expressed by cells with macrophage morphology (Fig. 1e). We observed few to no cells expressing PD-L1 in samples from patients with encephalitis of other etiologies (Supplementary Table 3). These samples also showed minimal to no lymphocytic infiltration, suggesting that PD-L1 expression in the brain may represent an attempt to dampen lymphocyte-derived inflammation and injury. PD-1 was expressed at lower levels by infiltrating lymphocytes and pericytes, cells which surround the capillary and venular endothelium and help maintain the blood-brain barrier (Extended Data Fig. 4)¹⁰. This pattern of immune cell infiltration and exhaustion markers were reminiscent of that reported in two cases of fulminant ICI-induced myocarditis⁵.

We profiled other markers of immune exhaustion including CD223/LAG-3 (T cells), CD244/2B4 (natural killer (NK) cells) and CD160 (CD8⁺ T cells and NK cells) in the inflammatory microenvironment and histologically normal regions (Extended Data Fig. 5). LAG-3, and to a lesser degree CD244, were highly expressed in the inflamed region but absent in the uninflamed region. We identified CD160⁺ cells in both tissues, although present at a higher degree in the inflamed region. These results suggested that the infiltrating T cell population likely received negative costimulation after repeated antigen exposure.

As only formalin-fixed autopsy tissue was available, we used NanoString digital spatial profiling to analyze several regions of interest (ROIs) in the immune microenvironment (Fig. 2a, Methods). We selected 12 ROIs each from inflamed and adjacent unaffected tissue sections (Fig. 2b). This analysis demonstrated a high degree of T cell and cytotoxic activation, with large increases in CD4, CD8, CD3, Ki67, PD-L1, GZMB and CD45RO in the affected region and minimal increase in the B cell markers CD19 and CD20 (Fig. 2c). We extended this analysis across additional

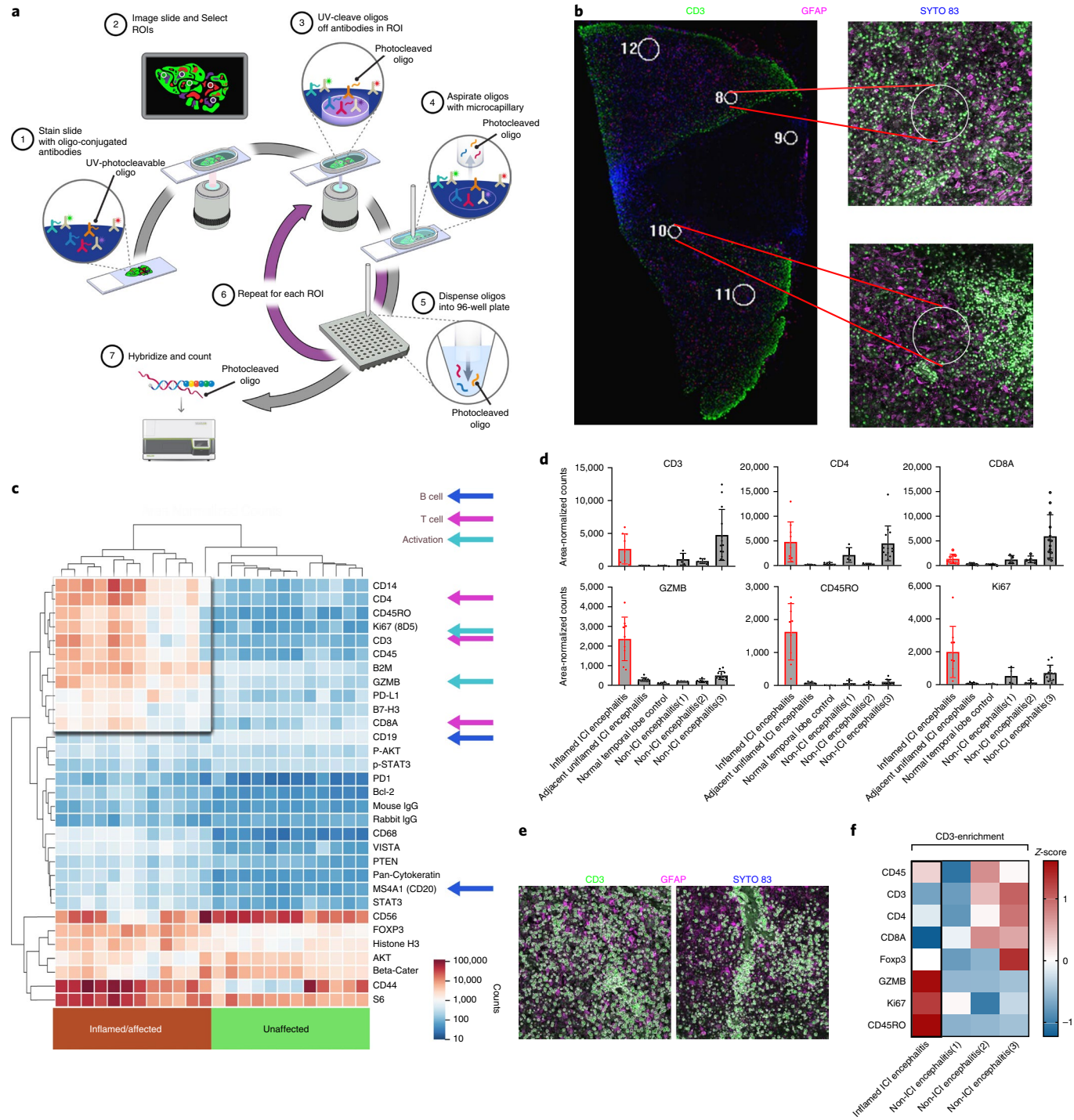


Fig. 2 | Digital spatial profiling of immune-related protein markers across inflamed and non-inflamed neural tissue. **a**, Schematic describing digital spatial profiling workflow. **b**, Representative ROI selection under immunofluorescence for analysis. Tissue was stained with anti-GFAP (pink) and anti-CD3 (green) in addition to SYTO 83 nuclear staining for ROI visualization and selection. Circular regions 200 μ m in diameter were excited with ultraviolet light to release barcodes for collection and analysis. Staining was repeated twice to verify results. **c**, Heatmap of area-normalized barcode counts from inflamed and unaffected tissue sections across 12 ROIs, one slide per tissue. Key antigens representing activation, T cell and B cell markers are identified by arrows. **d**, Spatio-regional protein expression patterns across 8–10 ROIs from brain tissues demonstrating enrichment for T cell markers in all encephalitis cases ($n=3$ non-ICI encephalitis cases), but only memory-activated markers in ($Ki67^{hi}$ $CD45RO^{hi}$ $GZMB^{hi}$) in ICI encephalitis ($n=1$); error bars represent mean \pm s.e.m. **e**, Representative images of $CD3^+$ T cells gated for barcode collection across two spatial ROIs in the inflamed region. **f**, Area-normalized counts represented by Z-score for each sample for key antigens demonstrating enrichment of memory-activated phenotypes ($Ki67^{hi}$ $CD45RO^{hi}$ $GZMB^{hi}$) in $CD3^+$ population ROIs (two ROIs on each of one slide/case) from ICI-induced encephalitis versus non-ICI encephalitis.

tissue controls, including a normal temporal lobe specimen and three cases of non-ICI-associated encephalitis (Supplementary Table 3). T cell infiltrate (CD3/4/8) was variable but similar across

affected tissue in both the present case as well as the non-ICI encephalitic cases; however, there was a preponderance of markers of activated memory phenotypes (expression of GZMB, CD45RO

and Ki67) in the present case (Fig. 2d). We next asked what markers were specifically enriched on the infiltrating T cell population, selecting two CD3⁺ T cell-specific ROIs on the inflamed region of the brain, as well as non-ICI encephalitic cases (Fig. 2e). While CD3 is expected to be enriched in these ROIs based on its use of fluorescently-labeled selection markers, this analysis further localized Ki67, CD45RO and GZMB specifically to T cells (Fig. 2f). Altogether, we reasoned that activated memory T cells were likely playing an important role in the pathophysiology.

Using RNA-seq and CIBERSORT analysis (see Methods), we observed several key changes in the inflamed region: (1) conversion of naïve CD4 cells to CD4 memory-activated T cell population in the inflamed tissue, (2) conversion from resting to activated mast cells, (3) a loss of memory B cells and (4) differentiation of M0 to M1/M2 macrophage phenotypes (Extended Data Fig. 6a). As a response to anti-PD-1 therapy has been linked to type-II interferon (IFN) responses, we asked whether IFN- γ -inducible genes were also over-represented in the inflamed region. Such genes were markedly upregulated (Extended Data Fig. 6b; Source Data Extended Data Fig. 6).

To quantify the clonality of these infiltrating T cells, we performed TCR β CDR3 sequencing using the immunoSEQ and ArcherDX platforms on: (1) the inflamed and unaffected regions of the brain, (2) prior resections of the tumor-adjacent lymph node, mesentery and metastasis to the brain and (3) the recurrence scar and spleen. The inflamed section demonstrated a high T cell fraction (71% of nucleated cells, Fig. 3a) and high degree of productive T cell clonality (0.369, Fig. 3b,c). Notably, a single TCR β sequence comprised 19.6% of all infiltrating T cells (CDR3 amino acid CASSFPGSYEQYF, Fig. 3d), with two other high-frequency clones comprising 5.98% and 5.91% of infiltrating T cells respectively. For comparison, the most prevalent clone infiltrating the cardiac muscle of two patients with myocarditis⁵ was approximately 9% (compared with 19.6% in this case of encephalitis). We detected this dominant clone at 1.08% in the spleen and 6.44% in the recurrence scar, though analyses of the TCR repertoire of additional tissues revealed mostly unique repertoires in comparison with the brain (Extended Data Fig. 7).

We performed six-digit HLA typing (see Methods and Supplementary Table 4) on the index case to leverage existing databases of TCR-antigen specificity and provide a contextual understanding of the TCR repertoire. Bioinformatic analyses (see Methods) revealed: (1) a PSGS motif expanded in the TCR repertoire in the inflamed brain found exclusively in TCRs recognizing viral proteins and not autoimmune TCRs (Supplementary Table 5) and (2) TCR CDR3 β sequences identical to known EBV-specific TCRs. Further query of publicly available databases (see Methods) revealed 23 further EBV-specific TCRs, including seven that exactly matched known HLA-A2-restricted EBV-specific TCRs that were previously described as specific to the epitopes GLC (BMLF1) and YLV (BRLF1)^{11–17}. These sequences represented 10.9% of infiltrating T cells in the inflamed region of the brain, including the second

most dominant TCR (Fig. 3e,f). We observed these sequences at frequencies higher than those found in acute-phase infectious mononucleosis patients and in the synovial fluid of rheumatoid arthritis patients, in whom these TCRs were first detected at frequencies of 5% of CD8⁺ T cells¹¹. While the frequency of these EBV-specific sequences fell to less than 1% of CD8⁺ T cells over time in acutely infected patients in those studies, we observed a distinct increase in the frequency of EBV-specific sequences in multiple tissues of the index case over time (Fig. 3g). These sequences also occupied 16.1% of sequences detected in the spleen biopsy of this patient and 5% of the brain recurrence scar. Notably, we did not detect any previously described HLA-A2-restricted or HLA-restriction-unknown TCRs specific to MelanA epitopes (see Methods).

Given consistent findings in our earlier data suggesting a predominance of CD4 memory-activated T cells in the inflamed region, we performed dual RNA in situ analysis (using an RNA probe specific to the oligoclonal RNA sequence) and immunohistochemistry (IHC) to characterize the cells. This analysis surprisingly yielded a complete localization of CASSFPGSYEQYF⁺ cells to CD4⁺ T cells (Fig. 3h). Furthermore, these CD4⁺ cells were also GZMB⁺ (40%), CD45RO⁺ (55%) and Ki67⁺ (10–15%) (Fig. 3i–k). Thus, the oligoclonal cells detected by TCR β sequencing are likely the same cells identified by digital spatial analysis and CIBERSORT, together corroborating that CD4 memory-activated T cells played a key role in this syndrome. Importantly, the second dominant TCR sequence (CASSRGQGSADTQYF), recognizing immediate-early HLA-A2-restricted epitopes GLC (BMLF1) and YLV (BRLF1), was found specifically in CD8⁺ T cells as expected and also colocalized with markers of activation (Fig. 3j and Extended Data Fig. 8).

Given the persistently positive EBV polymerase chain reaction from multiple CSF samples and EBV-specific TCR β sequences (reported below) identified in the brain, we performed a diagnostic RNA in situ hybridization (RNA-ISH) stain against EBV-encoded RNAs (*EBER1/2*). We identified rare but replicable EBER⁺ lymphocytes in the cortex and meninges (Extended Data Fig. 9a,b, respectively) of the affected region of the brain. *EBNA1*-specific RNA-ISH confirmed the presence of EBV-infected cells (Extended Data Fig. 9c,d). Staining of a lymph node dissection anteceding pembrolizumab indicated the presence of EBER⁺ cells, suggesting that the encephalitis did not arise from acute infection (Extended Data Fig. 9e). Surprisingly, EBER staining of the patient's resected brain metastasis, also pre-dating immunotherapy and symptoms, identified rare melanoma cells with EBER reactivity (Extended Data Fig. 9f). *EBNA1* staining of nine additional non-immunotherapy related encephalitis cases demonstrated complete absence of EBER⁺ lymphocytes in all cases, suggesting that EBV⁺ lymphocyte presence is an uncommon finding in cases of encephalitis caused by other etiologies (Supplementary Table 3). Notably, archival neural tissue from two other cases of ICI encephalitis, with substantially less robust inflammation, had negative EBER staining (Extended Data Fig. 10).

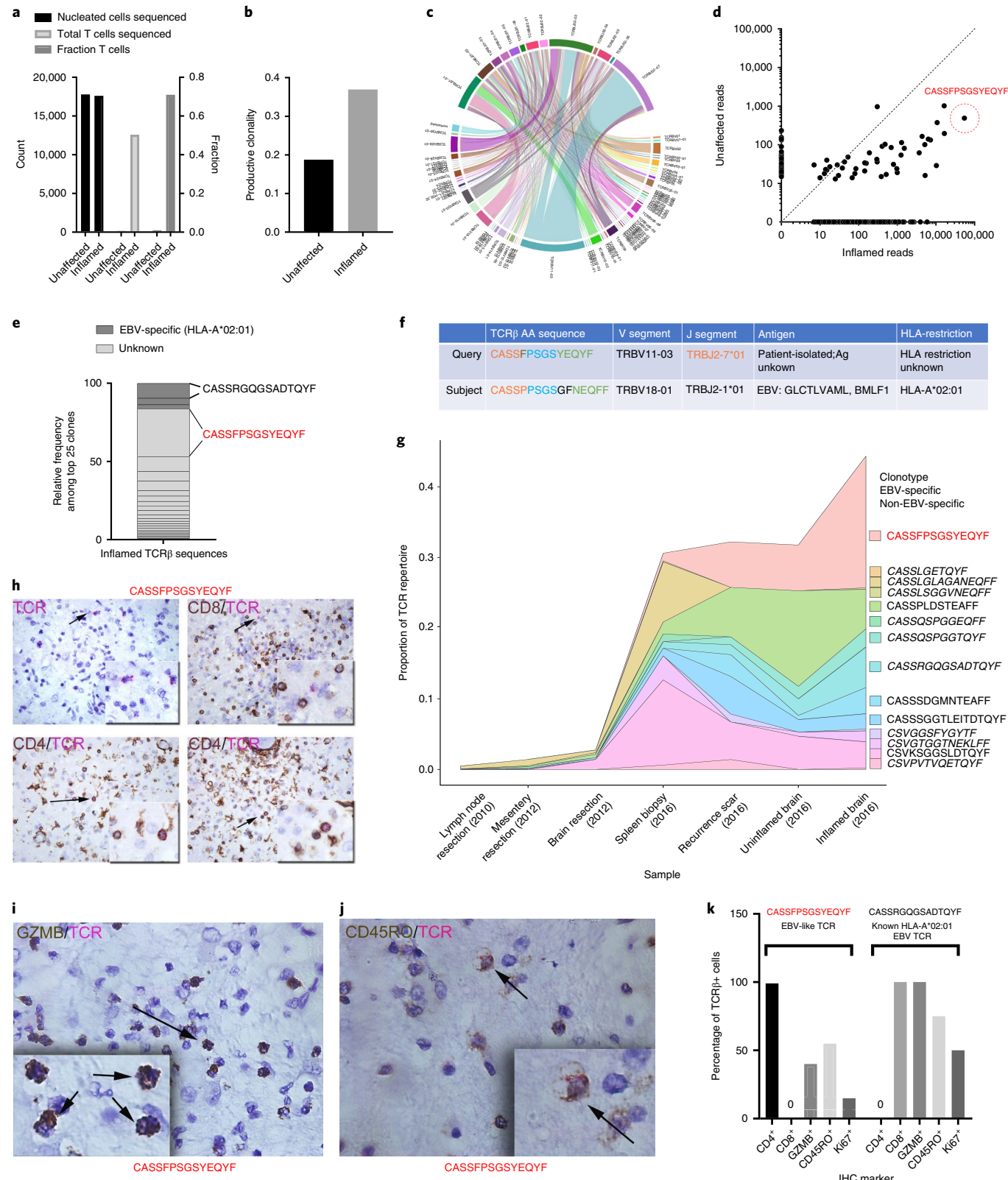
The molecular basis of ICI toxicity is unclear and difficult to analyze as such cases seem to arise stochastically. While these

Fig. 3 | TCR sequencing identification of oligoclonal CD4⁺ cytotoxic T cells in inflamed encephalitic tissue. **a**, ImmunoSEQ statistics of total cellular content, composition (fraction of T cells) and total T cells sequenced in inflamed and unaffected neural tissue. **b**, Enrichment of productive clonality in inflamed region of encephalitic tissue. **c**, Circos plot depicting the V(D)J rearrangements in TCR β in the repertoire. **d**, Biplot demonstrating enrichment of shared TCRs among the unaffected (likely regional presence) and inflamed tissues. The amino acid sequence predicted from the most highly represented DNA sequence is identified (CASSFPGSYEQYF). **e**, Representation of the top 25 clones according to known EBV-specificity based on patient HLA-type. **f**, Sequence similarity in TCR β amino acid sequence to a known EBV clone with specificity for the immediate-early HLA-A2-restricted epitopes GLC (BMLF1). **g**, Clonotype tracking over time and across tissue samples of EBV-specific and non-EBV-specific dominant clones found in the inflamed brain tissue. **h**, Dual IHC/RNA-ISH analysis for CD4/CD8 and EBV-like CASSFPGSYEQYF RNA sequence. Upper left: only the TCR probe (pink); upper right: exclusion of TCR probe with CD8⁺ T cells, lower: co-expression of CD4 with TCR probe. Stains and analysis were repeated twice for each case. **i**, Co-expression of granzyme B with TCR probe. Stains and analysis were repeated twice for each case. **j**, Co-expression of CD45RO with TCR probe. Stains and analysis were repeated twice for each case. **k**, Quantification for Ki67, CD45RO and granzyme B (GZMB) expressed as percent of all CASSFPGSYEQYF TCR β ⁺ cells, or the comparator CASSRGQGSADTQYF TCR β sequence, a known HLA-A*02:01 restricted EBV clone. Stains and analysis were repeated twice for each case.

Toxicities can affect nearly all organ systems, encephalitis is the most common neurological toxicity associated with ICI therapy¹⁸. Here, we report the clinical and molecular features of a fulminant and fatal case of anti-PD-1-induced encephalitis. Analyses of affected brain tissue demonstrated robust and clonal infiltration of cytotoxic CD4⁺ activated memory T cells, PD-L1 expression and evidence of

concurrent EBV infection. To our knowledge, this is the first molecular description of immune-therapy-induced neurotoxicity with a suggestion of interplay between viral infection and irAEs.

The cellular mechanisms of ICI toxicity remain poorly characterized. We and others have suggested that causes or correlations could include shared antigens present in tumor and affected tissue⁵,



pre-existing subclinical autoimmune responses^{19,20}, early B cell changes²¹ and specific intestinal microbiota²². We observed an extremely clonal cytotoxic CD4⁺ T cell population in this sample. Such cells have central roles in autoimmunity²³, anti-tumor immunity^{24,25} and antiviral defense^{26,27}. We cannot exclude the possibility that the clone we describe above is restricted by HLA-A2, as CD4⁺ T cells restricted by HLA class I and CD8⁺ T cells restricted by HLA class II have been described in numerous healthy and disease states^{28–31}. The frequency and phenotype of the CD4⁺ clone described above may suggest a new role for cytotoxic memory CD4⁺ T cells with respect to tumor control and dangerous autoreactivity as shown by others^{24,25}. Indeed, select TCRs are restricted by peptides presented on both HLA class I and class II, implying that such TCRs possess multiple specificities³². The presence and frequency of both CD4⁺ and CD8⁺ cytotoxic T cell populations in the brain and tumor microenvironment merit further study in additional cancer types and in autoimmune models, particularly given that the additional cases we examined both showed marked inflammation-associated T cell infiltration of the CNS. Further studies are also needed to determine the best interventions for prevention and management of these rare but fulminant toxicities.

Online content

Any methods, additional references, Nature Research reporting summaries, source data, statements of code and data availability and associated accession codes are available at <https://doi.org/10.1038/s41591-019-0523-2>.

Received: 10 May 2019; Accepted: 12 June 2019;

Published online: 22 July 2019

References

- Darvin, P., Toor, S. M., Sasidharan Nair, V. & Elkord, E. Immune checkpoint inhibitors: recent progress and potential biomarkers. *Exp. Mol. Med.* **50**, 165 (2018).
- Johnson, D. B., Chandra, S. & Sosman, J. A. Immune checkpoint inhibitor toxicity in 2018. *JAMA* **320**, 1702–1703 (2018).
- Postow, M. A., Sidlow, R. & Hellmann, M. D. Immune-related adverse events associated with immune checkpoint blockade. *N. Engl. J. Med.* **378**, 158–168 (2018).
- Moslehi, J. J., Salem, J.-E., Sosman, J. A., Lebrun-Vignes, B. & Johnson, D. B. Increased reporting of fatal immune checkpoint inhibitor-associated myocarditis. *Lancet* **391**, 933 (2018).
- Johnson, D. B. et al. Fulminant myocarditis with combination immune checkpoint blockade. *N. Engl. J. Med.* **375**, 1749–1755 (2016).
- Naidoo, J. et al. Pneumonitis in patients treated with anti-programmed death-1/programmed death ligand 1 therapy. *J. Clin. Oncol.* **35**, 709–717 (2017).
- Gonzalez, R. S. et al. PD-1 inhibitor gastroenterocolitis: case series and appraisal of ‘immunomodulatory gastroenterocolitis’. *Histopathology* **70**, 558–567 (2017).
- Verschuren, E. C. et al. Clinical, endoscopic, and histologic characteristics of ipilimumab-associated colitis. *Clin. Gastroenterol. Hepatol.* **14**, 836–842 (2016).
- Larkin, J. et al. Neurologic serious adverse events associated with nivolumab plus ipilimumab or nivolumab alone in advanced melanoma, including a case series of encephalitis. *Oncologist* **22**, 709–718 (2017).
- Rustenhoven, J., Jansson, D., Smyth, L. C. & Dragunow, M. Brain pericytes as mediators of neuroinflammation. *Trends Pharmacol. Sci.* **38**, 291–304 (2017).
- Annels, N. E., Callan, M. F., Tan, L. & Rickinson, A. B. Changing patterns of dominant TCR usage with maturation of an EBV-specific cytotoxic T cell response. *J. Immunol.* **165**, 4831–4841 (2000).
- Lim, A. et al. Frequent contribution of T cell clonotypes with public TCR features to the chronic response against a dominant EBV-derived epitope: application to direct detection of their molecular imprint on the human peripheral T cell repertoire. *J. Immunol.* **165**, 2001–2011 (2000).
- Cohen, G. B. et al. Clonotype tracking of TCR repertoires during chronic virus infections. *Virology* **304**, 474–484 (2002).
- Koning, D. et al. In vitro expansion of antigen-specific CD8(+) T cells distorts the T-cell repertoire. *J. Immunol. Methods* **405**, 199–203 (2014).
- Grant, E. J. et al. Lack of heterologous cross-reactivity toward HLA-A*02:01 restricted viral epitopes is underpinned by distinct $\alpha\beta$ T cell receptor signatures. *J. Biol. Chem.* **291**, 24335–24351 (2016).
- Dash, P. et al. Quantifiable predictive features define epitope-specific T cell receptor repertoires. *Nature* **547**, 89–93 (2017).
- Glanville, J. et al. Identifying specificity groups in the T cell receptor repertoire. *Nature* **547**, 94–98 (2017).
- Wang, D. Y. et al. Fatal toxic effects associated with immune checkpoint inhibitors: a systematic review and meta-analysis. *JAMA Oncol.* **4**, 1721–1728 (2018).
- Iwama, S. et al. Pituitary expression of CTLA-4 mediates hypophysitis secondary to administration of CTLA-4 blocking antibody. *Sci. Transl. Med.* **6**, 230ra45 (2014).
- Osorio, J. C. et al. Antibody-mediated thyroid dysfunction during T-cell checkpoint blockade in patients with nonsmall cell lung cancer. *Ann. Oncol.* **28**, 583–589 (2017).
- Das, R. et al. Early B cell changes predict autoimmunity following combination immune checkpoint blockade. *J. Clin. Invest.* **128**, 715–720 (2018).
- Dubin, K. et al. Intestinal microbiome analyses identify melanoma patients at risk for checkpoint-blockade-induced colitis. *Nat. Commun.* **7**, 10391 (2016).
- Peeters, L. M. et al. Cytotoxic CD4⁺ T cells drive multiple sclerosis progression. *Front Immunol.* **8**, 1160 (2017).
- Curran, M. A. et al. Systemic 4-1BB activation induces a novel T cell phenotype driven by high expression of eomesodermin. *J. Exp. Med.* **210**, 743–755 (2013).
- Hirschhorn-Cymerman, D. et al. Induction of tumoricidal function in CD4⁺ T cells is associated with concomitant memory and terminally differentiated phenotype. *J. Exp. Med.* **209**, 2113–2126 (2012).
- Penaloza-MacMaster, P. et al. Vaccine-elicited CD4 T cells induce immunopathology after chronic LCMV infection. *Science* **347**, 278–282 (2015).
- Takeuchi, A. & Saito, T. CD4 C. T. L., a cytotoxic subset of CD4⁺ T Cells, their differentiation and function. *Front Immunol.* **8**, 194 (2017).
- Ranasinghe, S. et al. Antiviral CD8⁺ T cells restricted by human leukocyte antigen class II exist during natural HIV infection and exhibit clonal expansion. *Immunity* **45**, 917–930 (2016).
- Boyle, L. H., Goodall, J. C. & Gaston, J. S. H. Major histocompatibility complex class I-restricted alloreactive CD4⁺ T cells. *Immunology* **112**, 54–63 (2004).
- Wang, M. et al. High-affinity human leucocyte antigen class I binding variola-derived peptides induce CD4⁺ T cell responses more than 30 years post-vaccinia virus vaccination. *Clin. Exp. Immunol.* **155**, 441–446 (2009).
- Legoux, F. et al. Characterization of the human CD4(+) T-cell repertoire specific for major histocompatibility class I-restricted antigens. *Eur. J. Immunol.* **43**, 3244–3253 (2013).
- Heemskerk, M. H. et al. Dual HLA class I and class II restricted recognition of alloreactive T lymphocytes mediated by a single T cell receptor complex. *Proc. Natl Acad. Sci. USA* **98**, 6806–6811 (2001).

Acknowledgments

We thank the patients and their families for participating in this study. W.J.M. was supported by NHBLI grant no. T32HL069765, NIDDK grant nos. R01DK112262 and R56DK108352 and NHLBI grant no. K12HL143956. S.A.M. was supported by NIAID grant no. P30AI110527. D.B.J. is supported by NIH/NCI grant no. K23 CA204726 and the James C. Bradford Jr. Melanoma Fund. J.E.S. was supported by the Cancer ITMO of the French National Alliance for Life and Health Sciences (AVIESAN). Plan Cancer 2014–2019. J.M.B. was supported by the Department of Defense Era of Hope Award no. BC170037 and NIH/NCI grant no. R00CA181491. In addition, we acknowledge the Translational Pathology Shared Resource supported by NCI/NIH Cancer Center Support Grant no. P30 CA68485–19 and the Vanderbilt Mouse Metabolic Phenotyping Center Grant no. U24 DK059637–16. The supplied data from VigiBase come from a variety of sources. The probability that a reported adverse event is related to a drug response is not equal in all cases; the information in VigiBase and these analyses does not represent the opinion of the World Health Organization or the Uppsala Monitoring Centre.

Author contributions

D.B.J., W.J.M. and J.M. Balko conceptualized the study. W.J.M., P.I.E.-G., J.S., K.B., Y.L., S.W. and J.M. Beecham developed the methodology. Software was designed by W.J.M. and J.M. Balko. D.B.J., W.J.M., P.I.E.-G., K.B., Y.L., S.W., J.B. and J.M. Beecham were in charge of validation. D.B.J., W.J.M., Y.W., Y.X. and J.M. Balko performed the formal analysis. C.A.C., D.Y.W., D.B.J., W.J.M., P.I.E.-G. and J.M. Balko led the investigation. Resources were sourced by R.A.-R., B.C.M., C.S., J.-E.S., A.M.M., M.T., G.V.L., J.V.C., A.C.G., M.O., S.C., A.C., B.L.-V., S.M.G., E.J.R., E.I.B., S.A.M., M.E.S., J.J.M., J.A.S. and J.M. Balko. D.B.J., D.Y.W., W.J.M., J.-E.S., Y.W., Y.X. and J.M. Balko curated the data. D.B.J., W.J.M. and J.M. Balko wrote the original draft. All authors reviewed and edited the paper. D.B.J., W.J.M. and J.M. Balko visualized the study. D.B.J., W.J.M. and J.M. Balko supervised the project and were in charge of its administration. Funding acquisition was done by D.B.J. and J.M. Balko.

Competing interests

K.B., J.B., Y.L. and S.W. are employees of NanoString and receive compensation as such. D.J. serves on advisory boards for Array, Bristol Myers Squibb, Genoptix, Incyte and Merck, and has received research funding from Bristol Myers Squibb and Incyte. J.M.B. receives consulting fees from Novartis and research support from Genentech and Incyte. J.J.M. serves as a consultant or in an advisory role for BMS, Daiichi Sankyo, Novartis, Pfizer, Regeneron, Takeda, Myokardia, Deciphena and Ipsen, and has received research funding from BMS and Pfizer. C.A.C. receives grant/research funding from Gilead Sciences, Inc. (related to hepatitis C virus). A.M.M. serves on advisory boards for Bristol Myers Squibb, Merck Sharpe and Dohme, Novartis, Roche, and Pierre-Fabre. E.I.B. serves on advisory boards for Bristol Myers Squibb and Novartis. G.V.L. reports receiving fees for serving on advisory boards of Aduro, Amgen, Array Biopharma, Bristol-Myers Squibb, Merck Sharp and Dohme (a subsidiary of Merck & Co., Inc., Kenilworth, NJ, USA), Novartis, Oncosec, Pierre Fabre and Roche.

Additional information

Extended data is available for this paper at <https://doi.org/10.1038/s41591-019-0523-2>.

Supplementary Information is available for this paper at <https://doi.org/10.1038/s41591-019-0523-2>.

Reprints and permissions information is available at www.nature.com/reprints.

Correspondence and requests for materials should be addressed to D.B.J. or J.M.B.

Peer review information: Saheli Sadanand was the primary editor on this article and managed its editorial process and peer review in collaboration with the rest of the editorial team.

Publisher's note: Springer Nature remains neutral with regard to jurisdictional claims in published maps and institutional affiliations.

© The Author(s), under exclusive licence to Springer Nature America, Inc. 2019

Methods

Index patient and autopsy data. The index patient consented to protocols that permitted de-identified research use of biospecimens, genetic testing results and clinical data (Vanderbilt IRB numbers 100178, 181685 and 030220) and his family consented to a postmortem histopathologic evaluation; cases from outside institutions were approved with institution-specific protocols. Clinical data were obtained through chart review. During the autopsy, evaluation for melanoma using standard melanoma stains (MITF, MelanA, SOX10, S100), and histopathologic evaluation of infiltrating immune cell subsets using CD3, CD20 and CD68 was performed in accordance with institutional protocols.

Additional cases of checkpoint inhibitor-associated encephalitis. Additional case 1 was seen at the University Hospital, Zurich, Switzerland and has been previously described³³. Briefly, she was a 60-year-old (in 2012) patient with an isolated lesion in the right gyrus frontalis medius as well as bilateral pulmonary metastases. After neurosurgical resection followed by adjuvant radiotherapy (with a total of 30 Gray (Gy)) the patient was treated with ipilimumab (3 mg kg⁻¹ intravenously) for a total of four doses. After 3 months from the last dose, the patient reported generalized tiredness, weakness and loss of appetite. Serum endocrinological work-up revealed a non-significant cortisol shift without osmolality changes, which was not specific for hypopituitarism or adrenal insufficiency. No new metastases were found in the MRI of the brain. A new positron emission tomography-computer tomography (CT) scan showed bilateral pulmonary progression. Subsequent therapy with pembrolizumab was initiated (one infusion). The patient died without any antecedent evidence of altered physical status within 2 weeks. At autopsy, gross inspection revealed a 3 cm defect in the right frontal lobe. No other lesions were seen on further sectioning. Microscopic examination was remarkable for scattered perivascular and parenchymal collections of mature lymphocytes, mostly CD8⁺ T cells, in the hemispheres and brainstem. In addition, sections of brainstem showed CD68⁺ microglial cells, occasionally organized in loose nodules. IHC preparations for cytomegalovirus, HSV I and II, simian virus 40, toxoplasmosis and varicella zoster virus were negative. There was evidence of melanoma metastasis, even after additional sampling. A diagnosis of encephalitis was rendered based on the presence of intraparenchymal and perivascular CD8⁺ lymphocytes accompanied by microglial proliferation.

Additional case 2 was seen at Dana–Farber Cancer Institute in Boston, MA, USA and initially presented in 2013 with a T1a melanoma of the left lower extremity. He was followed until 2015 when he noted increased dyspnea on exertion and a CT scan showed numerous enlarged lymph nodes throughout the chest, abdomen and pelvis. The largest of these was a 7.4 × 5.3 cm² left pelvic sidewall node with numerous other large nodes noted. He underwent an ultrasound-guided biopsy which demonstrated metastatic melanoma. He was started on single-agent pembrolizumab and after the first dose started reporting increased tremors and leg weakness. Due to the subacute nature of these symptoms he received two more treatments with pembrolizumab with progressively worsening symptoms. He developed increased weakness and memory issues and the pembrolizumab was held and he was admitted for work-up of this. Lumbar puncture X3, MRI of the brain and spine, neurologic evaluation and extensive work-up for other causes of his symptoms was performed without an etiology. He received a short course of high-dose steroids followed by intravenous immunoglobulin and a longer steroid taper without benefit. His functional status continued to decline without a clear etiology despite these interventions and brain biopsy was performed which showed T cell inflammatory infiltrate and gliosis suspicious for pembrolizumab-related encephalopathy. He subsequently died from progressive neurologic decline.

Additional cases of encephalitis of other etiologies. Additional cases of encephalitis not associated with checkpoint inhibitor use were collected under an IRB-approved protocol to study cellular heterogeneity in normal brain and brain neoplasms (IRB no. 180238). Cases were stained with EBNA1 RNA-ISH and anti-PD-L1 IHC as detailed below. Details of the cases are listed in Supplementary Table 3. Positive and negative control probes were used in all cases to verify specificity and presence of intact RNA for analysis. See Reporting Summary for additional information.

Immunohistochemistry. Archival tissue from the autopsy was obtained and IHC evaluation was performed. Antibodies used were anti-CD45RO (Thermo Scientific, catalog no. MA5-11532, dilution 1:1,600), anti-GZMB (Granzyme B, Biocare, catalog no. ACI 3202 AA, prediluted), anti-Ki67 (Dako, catalog no. M7240, dilution 1:200), anti-CD4 (StatLab, catalog no. RM27-10, prediluted), anti-CD8 (StatLab, catalog no. MM39-10, prediluted), anti-PD-L1 (ThermoFisher, catalog no. PA5-28115, dilution 1:7500), anti-CD68 (Abcam, catalog no. ab125212, dilution 1:600), anti-PD-1 (Sigma-Aldrich, HPA035981, dilution 1:75), anti-CD20 (Leica, PA0906, prediluted), anti-LAG-3 (Cell Signaling, catalog no. 15372, dilution 1:200), CD244 (Proteintech, catalog no. 16677-1-AP, dilution 1:200), CD160 (Abcam, catalog no. ab202845, dilution 1:600). The Bond Polymer Refine detection system or Envision system was used for visualization. Slides were then dehydrated, cleared and coverslipped. See Reporting Summary for additional information.

RNA in situ hybridization (RNA-ISH) analysis.

For RNAscope RNA-ISH (Advanced Cell Diagnostics) analysis of EBNA1, standard RNAscope manufacturer's protocols were followed using the RNAscope H₂O₂ and protease pretreatment kit, (ACD, reference no. 322381), RNAscope Target retrieval buffer (ACD, reference no. 322000) and appropriate positive and negative RNA probes for controls. For custom BaseScope RNA-ISH (Advanced Cell Diagnostics) TCR β analysis (ACD, reference no. 712111), standard BaseScope manufacturer's protocols were followed using BaseScope Detection Reagents, RED (ACD, reference no. 322910). Dual ISH-IHC was performed using the custom TCR β target probe(s) followed by incubation with primary antibodies (CD4, CD8, Ki67, CD45RO and GZMB) as described above, using the Envision (Dako) system, DAB (Dako) and hematoxylin counterstain. For EBER staining, slides were placed on the Leica Bond Max IHC stainer and all steps, besides dehydration, clearing and coverslipping, were performed on the Leica Bond Max. Slides were deparaffinized, and enzyme retrieval was performed using Proteinase K (Dako, reference no. S3020) for 5 min. Slides were put through ISH hybridization with the Ready-To-Use EBER probe (Leica, reference no. ISH15687-A) for 2 h. Slides were placed in an anti-fluorescein antibody (Leica, reference no. AR0222) for 15 min. The Bond Polymer Refine detection system was used for visualization. Slides were then dehydrated, cleared and coverslipped. For dual staining, data were quantified by colocalization of the signal as a fraction of the TCR $^+$ cells, by a licensed pathologist (PIE-G).

RNA sequencing. Total RNA quality was assessed using the 2200 TapeStation (Agilent). At least 20 ng of DNase-treated total RNA having at least 30% of the RNA fragments with a size >200 nucleotides (DV200) was used to generate RNA Access libraries (Illumina) following manufacturer's recommendations. Library quality was assessed using the 2100 Bioanalyzer (Agilent) and libraries were quantitated using KAPA Library Quantification Kits (KAPA Biosystems). Pooled libraries were subjected to 75 base pair paired-end sequencing according to the manufacturer's protocol (Illumina HiSeq3000). Bcl2fastq2 Conversion Software (Illumina) was used to generate de-multiplexed FASTQ files.

Quality control (QC) for the paired-end raw sequencing reads of all samples were performed using FastQC³⁴ for the analysis of sequence quality, guanine-cytosine (GC) content, adapter content, over-represented k-mers and duplicated reads. Sequencing reads were mapped to human reference genome GRCh38 (Release-85, Ensembl) using STAR 2.2.1 with two-pass mapping³⁵. QC for read alignment and mapping was evaluated with RSeQC³⁶ for sequencing saturation, mapped reads clipping profile, mapped read distribution and coverage uniformity. Transcript-per-million values were calculated using RSEM³⁷ and used to assess the global quality and replicability of the RNA-seq data set and exported for downstream data analyses.

CIBERSORT and gene set analysis. CIBERSORT analysis was performed on RNA-seq transcript-per-million level data generated above, using both the 'relative' and 'absolute' methods available on the analysis website (<https://cibersort.stanford.edu/>). The CIBERSORT method used is explained in full detail elsewhere³⁸. To complete this analysis, we used the LM22 data set which was carefully developed and validated in the manuscript. The genes used, along with computational methods and development/validation approach are provided as supplemental data in the original report³⁸ and also freely available on the CIBERSORT website. Analysis was performed as previously described³⁸. For interferon gene set analysis, the HALLMARK_INTERFERON_GAMMA_RESPONSE (M5913; 200 genes, 177 genes in overlap/matching) signature was downloaded from the Molecular Signatures Database (<http://software.broadinstitute.org/gsea/msigdb>). For each gene, the log₂(fold change) was calculated between the inflamed and unaffected region, or across additional tissues as indicated.

TCR sequencing. TCR sequencing and clonality quantification was assessed in neuropathologist-selected (by B.M.) formalin-fixed, paraffin-embedded (FFPE) samples of highly inflamed and non-inflamed brain parenchyma using survey level immunoSEQ and the Immunoverse assay, as previously described (Adaptive Biotechnologies, ArcherDX)^{39,40}. Sequencing results were evaluated using the immunoSEQ analyzer, v.3.0. Shannon entropy, a measure of sample diversity, was calculated on the clonal abundance of all productive TCR sequences in the data set. Shannon entropy was normalized by dividing Shannon entropy by the logarithm of the number of unique productive TCR sequences. This normalized entropy value was then inverted (1 – normalized entropy) to produce the clonality metric.

TCR repertoire analysis: data processing. We processed raw immunoSEQ data for downstream analysis using VDJTools⁴¹. We excluded clonotypes if a TRBV or TRB β gene was not assigned or if they were non-productive. We then recalculated the frequency of each remaining productive sequence and collapsed the resulting TCR repertoire data set by CDR3 amino acid sequence (that is the counts for two clonotypes with different nucleotide sequences encoding the same CDR3 AA sequence would be summed).

TCR repertoire analysis: clonotype annotation and known antigen assignment. We first retrieved continuous and discontinuous CDR3 β motifs significantly

enriched at least threefold above a naïve repertoire of 200,000 unselected CD4 and CD8 T cells at a resampling depth of 10,000 using the GLIPH algorithm¹⁷. We then annotated each TCR repertoire for known and possible antigen specificity and pathogenic associations using the greedy VDJMatch algorithm⁴² in VDJDB against each CDR3β and significant motifs from GLIPH¹⁷ and a Levenshtein distance of 1 for sequences stored in McPAS-TCR⁴³. We also searched 2,460 HLA-A2 restricted previously published⁴⁴ melanoma-specific TCRs for matches and homology to our TCR repertoire data.

TCR repertoire analysis: *in silico* epitope prediction. Finally, we annotated each clonotype sequence for potential recognition of 38 viral and 5 cancer T cell epitopes using CDR3β sequence, *TRBV* gene and *TRBJ* gene as input to the random forest TCRex model⁴⁵ at a false positive rate of 1 in 10,000 (0.01%).

Pharmacovigilance database analysis. We queried VigiBase, the World Health Organization database of individual case safety reports containing more than 18 million individual case safety reports submitted by national pharmacovigilance centers since 1967, on 23 January 2018. These reports originate from sources including healthcare professionals, patients and pharmaceutical companies and are generally reported post-marketing. Of >18,000,000 individual reports, 47,240 were from patients receiving nivolumab, pembrolizumab, ipilimumab, atezolizumab, durvalumab, avelumab, or tremelimumab. We used the following Medical Dictionary for Regulatory Activities (MedDRA) preferred terms for encephalitis associated with ICI: encephalitis, encephalitis autoimmune, limbic encephalitis, meningoencephalitis and cerebellitis for the following drugs: nivolumab, pembrolizumab, ipilimumab, atezolizumab, durvalumab, avelumab and tremelimumab. We collected the date of report, therapy, indication (cancer type), age, sex, concurrent adverse events, time of onset and outcome for all patients when available. We used descriptive statistics to quantify medians and range for continuous variables and percentages for categorical variables. We used the R statistical language (v.3.5.1) to perform the χ^2 test for contingency tables.

Digital spatial profiling of protein. Single FFPE slides from inflamed and non-inflamed brain tissue were selected, as well as from non-inflammatory ‘healthy’ brain (epileptic) and three additional cases of non-ICI-induced encephalitis. Overall, ten ROIs within each slide were selected by pathologists (authors R.A. and B.M.). Multiplexed protein profiles were generated with the NanoString GeoMX digital spatial profiling platform (RUO—research use only). Formalin-fixed paraffin-embedded tissue sections of 5 μm thickness were subjected to antigen retrieval (citrate buffer pH6) and stained with a cocktail of antibodies labeled with photocleavable DNA-indexing oligos (to generate quantitative protein profiles), fluorescent anti-CD3 and anti-GFAP (visualization markers) and SYTO 83 nuclear dye (ThermoFisher, S11364). Tissues were imaged by fluorescence microscopy on the GeoMX platform and ROIs were chosen for molecular profiling. ROIs were selected as circles 200 μm in diameter from inflamed or healthy tissue or by custom masking using the fluorescent CD3 signal to specifically identify T cells and a digital micromirror device to precisely control the pattern of ultraviolet illumination. ROIs were exposed to ultraviolet light (365 nm) to release oligos which were captured via microfluidics and stored in individual wells of a microtiter plate. Following collection from all ROIs, oligos were hybridized to unique four-color, six-spot optical barcodes and enumerated on the nCounter platform. Data were normalized to ERCC-sequence specific probes to control for technical variation in hybridization efficiency, followed by area normalization to control for ROI size and control IgG (rabbit and mouse) to normalize for background. Data were visualized by unsupervised hierarchical clustering or grouped dot plots.

Statistics. All statistics were calculated using GraphPad Prism 8 and R v.3.5.1. We used GraphPad Prism 8 to test for significant differences in the IFN-γ gene signature using one-way analysis of variance with Tukey’s post hoc test to correct for multiple comparisons. We used GraphPad Prism 8 to calculate linear regressions shown in Extended Data Fig. 7, the r^2 and two-tailed F -test of non-zero slope and its 95% CI.

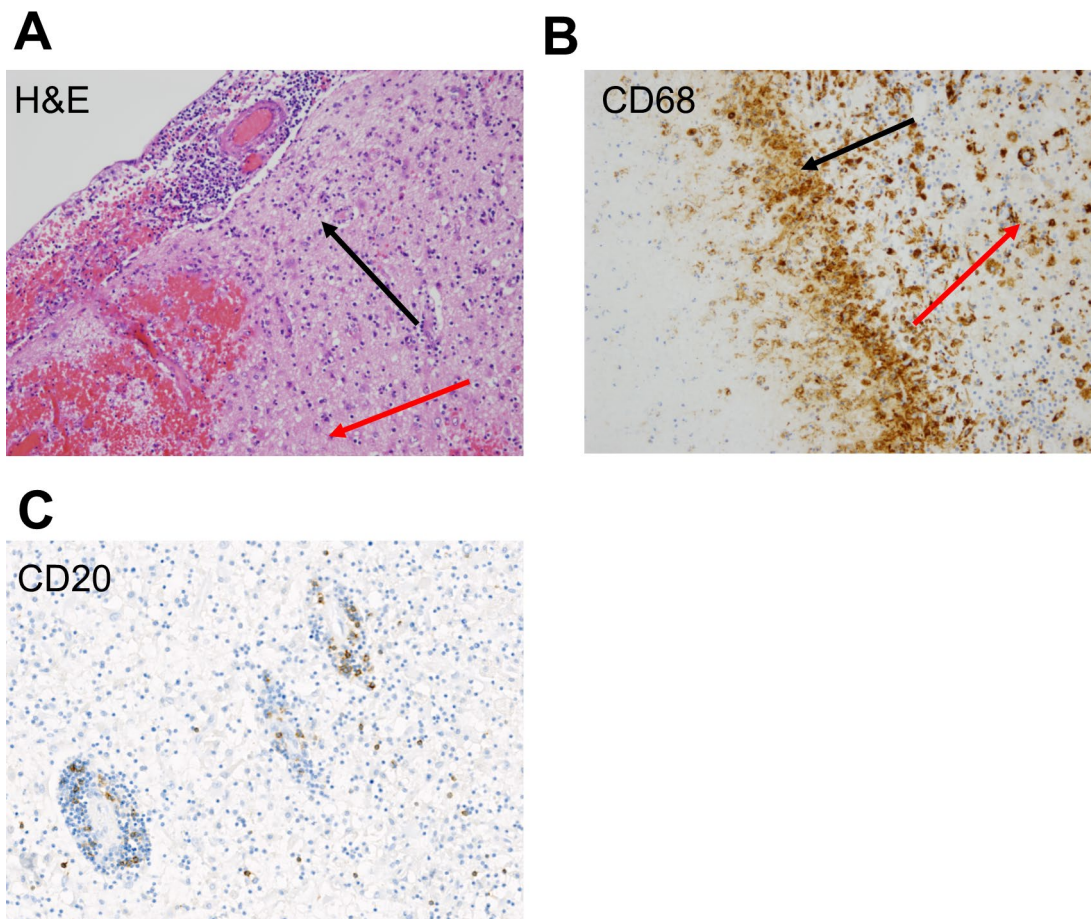
Reporting summary. Further information on research design is available in the Nature Research Reporting Summary linked to this article.

Data availability

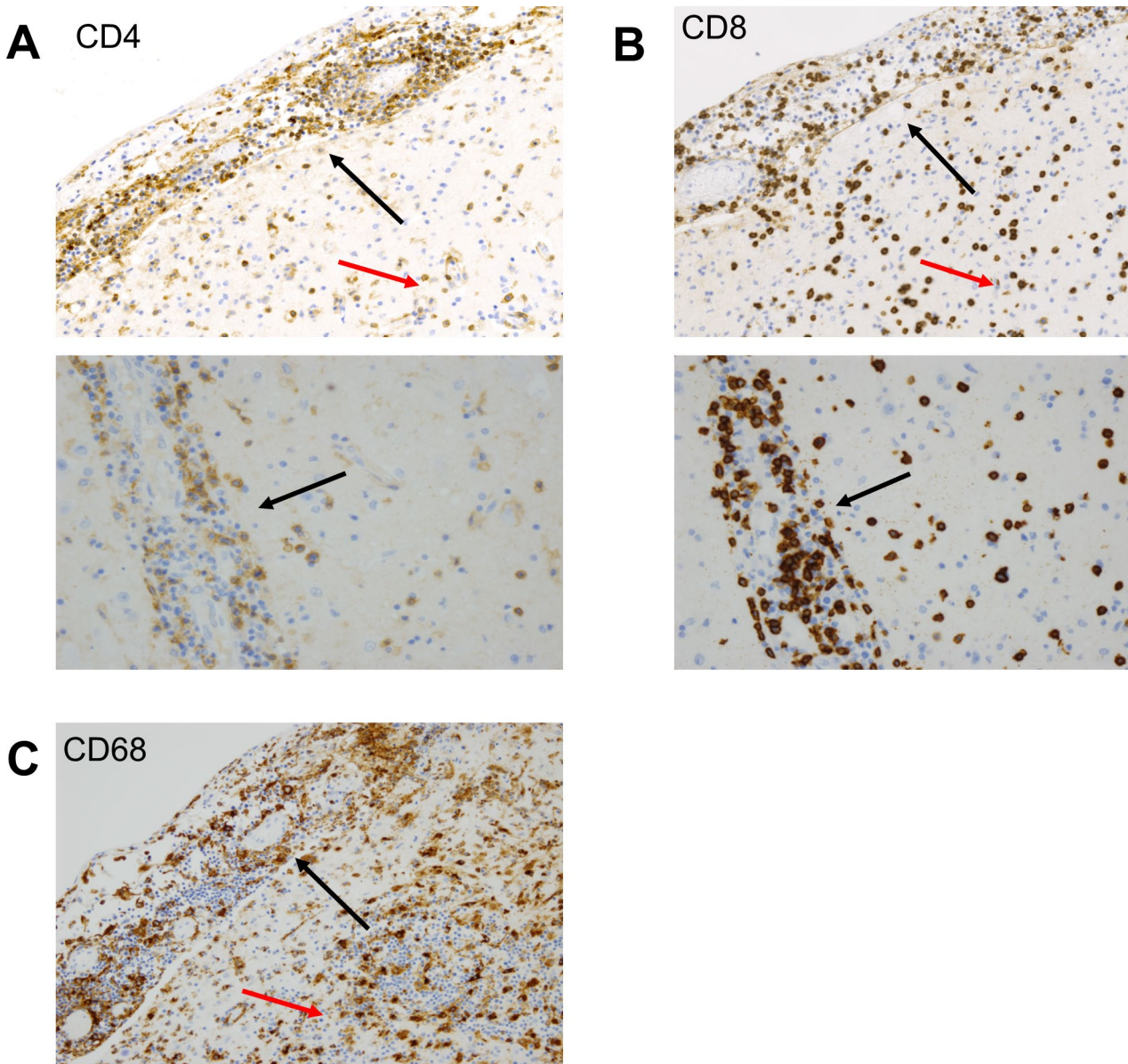
Source data for RNA-seq analyses (IFN-γ genes) are included as Supplementary Data Set 1. All other data, including processed TCR sequencing data, are available on request from the corresponding authors. The Center for Technology Transfer and Commercialization at Vanderbilt University Medical Center will promptly review all data requests to ensure that intellectual property and confidentiality obligations are met; a Material Transfer Agreement will be used to transfer any and all data that can be shared, including TCR sequencing data. RNA-seq data from this study have been deposited in the database of Genotypes and Phenotypes (https://prod.tbilab.org/balko_lab/encephalitis_NMED/).

References

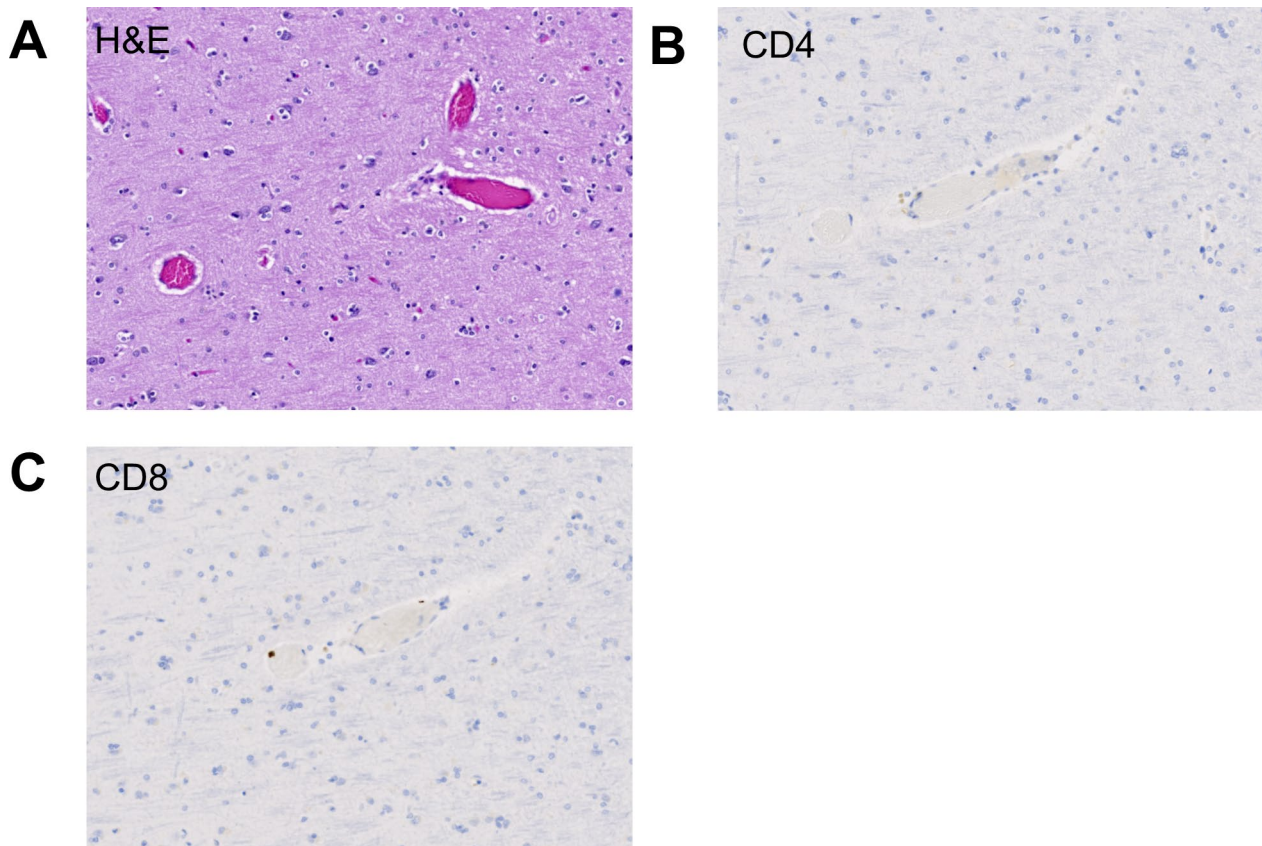
33. Bossart, S. et al. Case report: encephalitis, with brainstem involvement, following checkpoint inhibitor therapy in metastatic melanoma. *Oncologist* **22**, 749–753 (2017).
34. Andrews, S. FastQC: a quality control tool for high throughput sequence data. <http://www.bioinformatics.babraham.ac.uk/projects/fastqc> (2010).
35. Dobin, A. et al. STAR: ultrafast universal RNA-seq aligner. *Bioinformatics* **29**, 15–21 (2013).
36. Wang, L., Wang, S. & Li, W. RSeQC: quality control of RNA-seq experiments. *Bioinformatics* **28**, 2184–2185 (2012).
37. Li, B. & Dewey, C. N. RSEM: accurate transcript quantification from RNA-Seq data with or without a reference genome. *BMC Bioinforma.* **12**, 323 (2011).
38. Newman, A. M. et al. Robust enumeration of cell subsets from tissue expression profiles. *Nat. Methods* **12**, 453–457 (2015).
39. Tumeh, P. C. et al. PD-1 blockade induces responses by inhibiting adaptive immune resistance. *Nature* **515**, 568–571 (2014).
40. Mathew, J. M. et al. Generation and characterization of alloantigen-specific regulatory T cells for clinical transplant tolerance. *Sci. Rep.* **8**, 1136 (2018).
41. Shugay, M. et al. VDJtools: unifying post-analysis of T cell receptor repertoires. *PLoS Comput. Biol.* **11**, e1004503 (2015).
42. Shugay, M. et al. VDJdb: a curated database of T-cell receptor sequences with known antigen specificity. *Nucleic Acids Res.* **46**, D419–D427 (2018).
43. Tickotsky, N., Sagiv, T., Prilusky, J., Shifrut, E. & Friedman, N. McPAS-TCR: a manually curated catalogue of pathology-associated T cell receptor sequences. *Bioinformatics* **33**, 2924–2929 (2017).
44. Chen, G. et al. Sequence and structural analyses reveal distinct and highly diverse human CD8(+) TCR repertoires to immunodominant viral antigens. *Cell Rep.* **19**, 569–583 (2017).
45. Gielis, S. et al. TCRex: a webtool for the prediction of T-cell receptor sequence epitope specificity. Preprint at *bioRxiv* <https://doi.org/10.1101/373472> (2018).



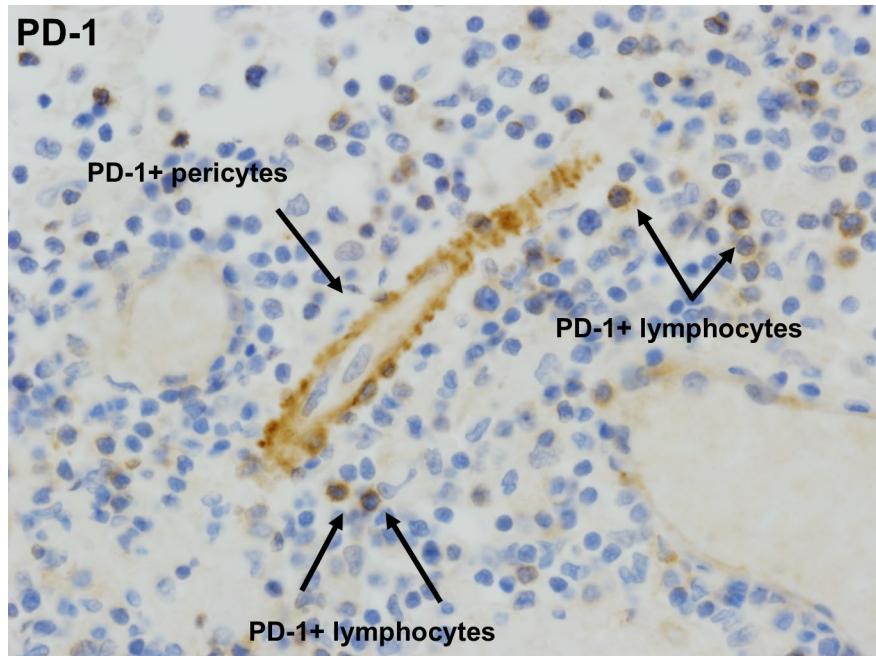
Extended Data Fig. 1 | Inflammatory and myeloid/microglial infiltrate in infarct regions of brain. **a**, H&E stain shows a dense chronic inflammatory infiltrate in the meninges (upper left; black arrow), focal hemorrhage in the underlining brain parenchyma (lower left; red arrow) and gliotic gray matter; $\times 20$ magnification. **b**, CD68 positive cells at the interface of the necrotic area (black arrow) and the adjacent brain parenchyma (red arrow); $\times 20$ magnification. **c**, Limited expression of CD20 staining in perivascular and parenchymal regions of brain; $\times 20$ magnification. Stains were performed once on a single tissue section with a batch-controlled positive and negative control.



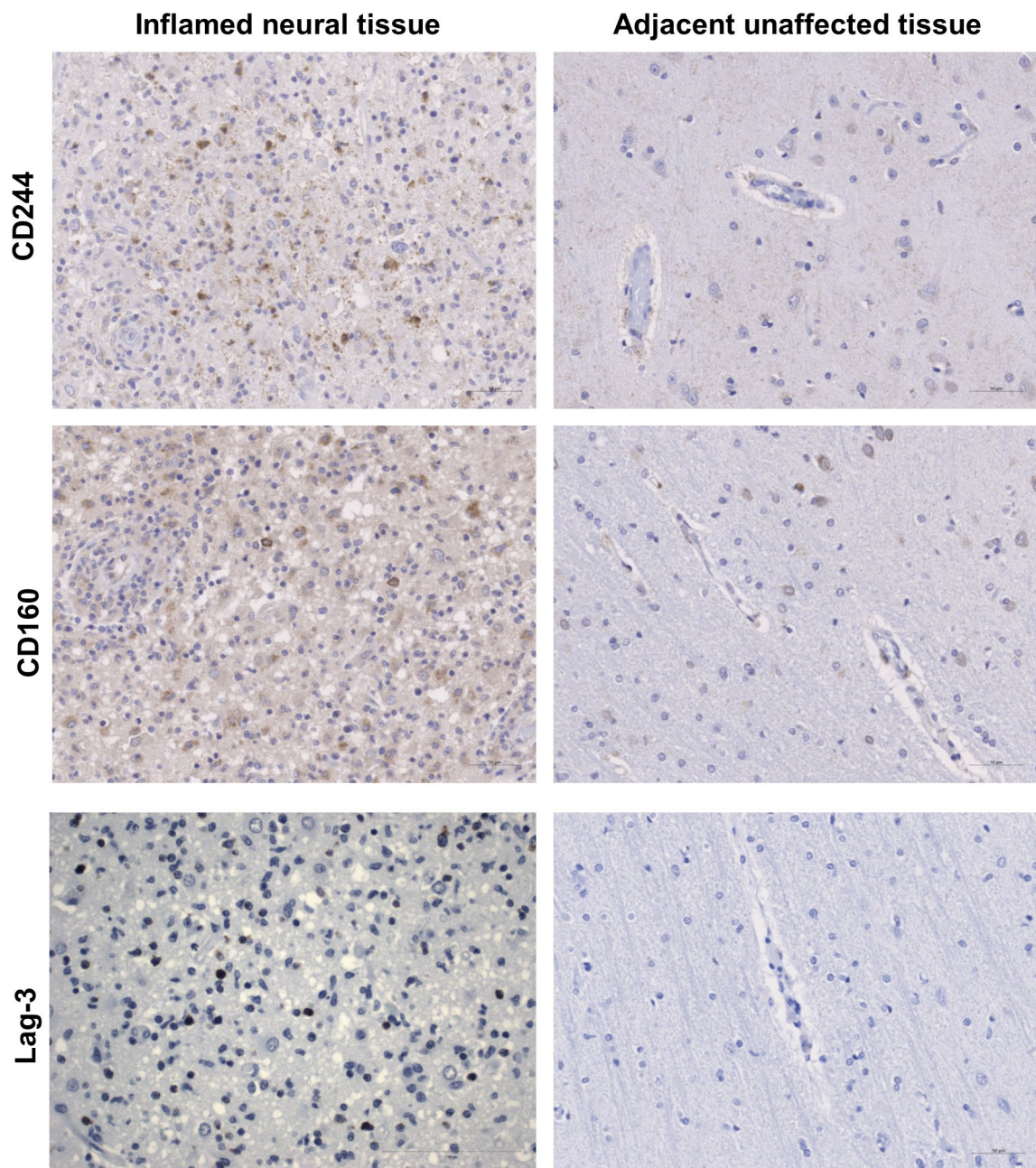
Extended Data Fig. 2 | Lymphocytic and myeloid infiltrate in meninges, perivascular and parenchymal regions. **a**, The lymphocytic infiltrate involving the meninges (upper left of image; upper left of image, black arrow), parenchyma and brain perivascular regions (upper image; lower right of image, red arrow and lower image) includes CD4. $\times 20$ magnification. **b**, CD8 $^{+}$ positive T cells; $\times 20$ magnification. **c**, CD68 positive cells accompanying lymphocytic infiltrate in meninges (upper left of image, black arrow) and brain parenchyma (lower right, red arrow); $\times 20$ magnification. Stains were performed once on a single tissue section with a batch-controlled positive and negative control.



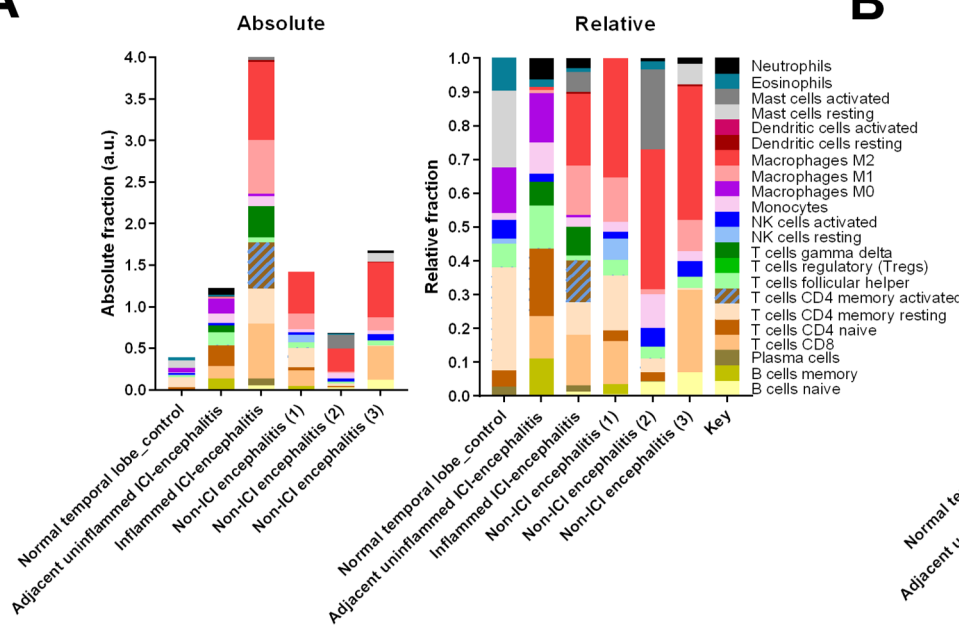
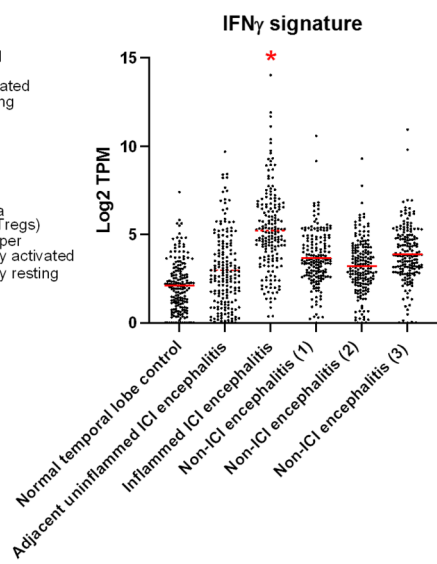
Extended Data Fig. 3 | Absence of substantial inflammatory infiltrate in radiologically and macroscopically non-affected area. **a**, H&E corresponding to radiologically and macroscopically non-affected area with preserved architecture and no apparent inflammatory infiltrate; $\times 20$ magnification. **b**, CD4. **c**, CD8 stains demonstrating sparse presence or absence of T cell infiltrates in radiologically and macroscopically non-affected area; $\times 20$ magnification. Stains were performed on a single tissue section with a batch-controlled positive and negative control.



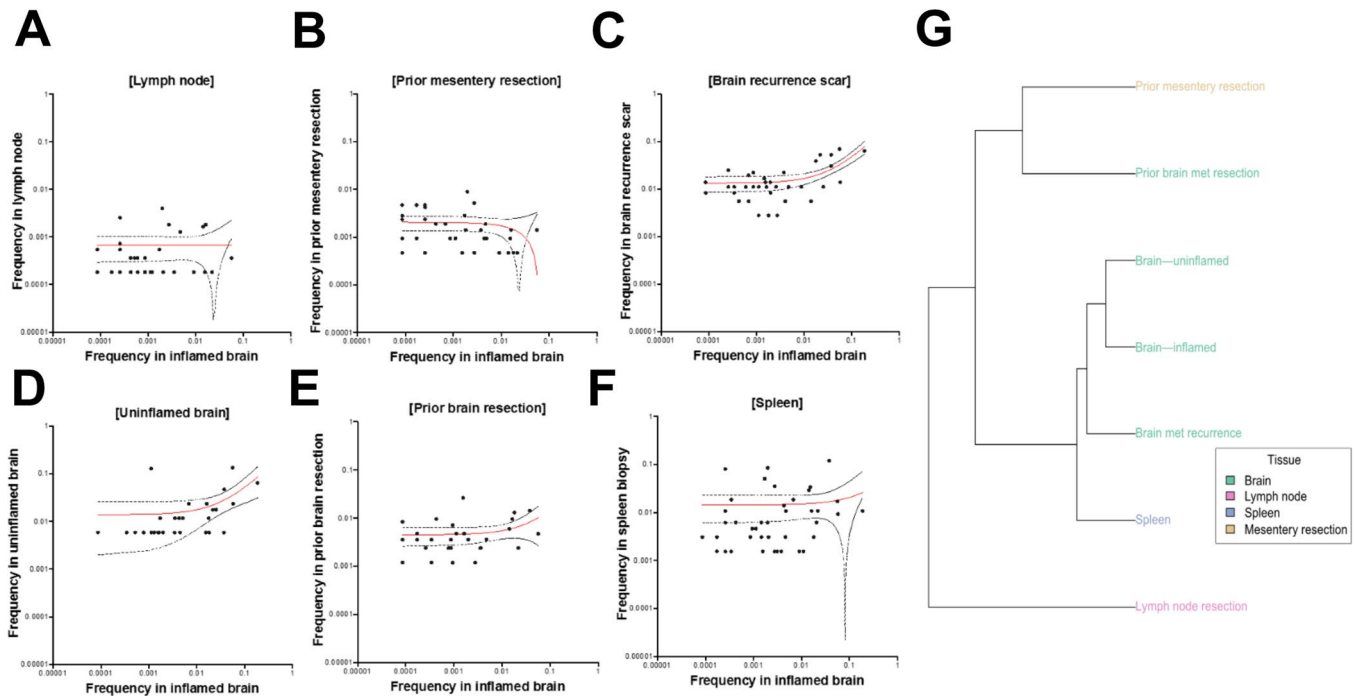
Extended Data Fig. 4 | PD-1 expression in inflamed region of brain. PD-1 positive perivascular lymphocytes and pericytes; $\times 20$ magnification. Stains were performed on a single tissue section with a batch-controlled positive and negative control.



Extended Data Fig. 5 | Expression of T cell and NK cell markers of immune cell exhaustion. Inflamed and non-inflamed adjacent regions of neural tissue were immunostained for CD244, CD160 and LAG-3; $\times 20$ magnification. Stains were performed on a single tissue section with a batch-controlled positive and negative control.

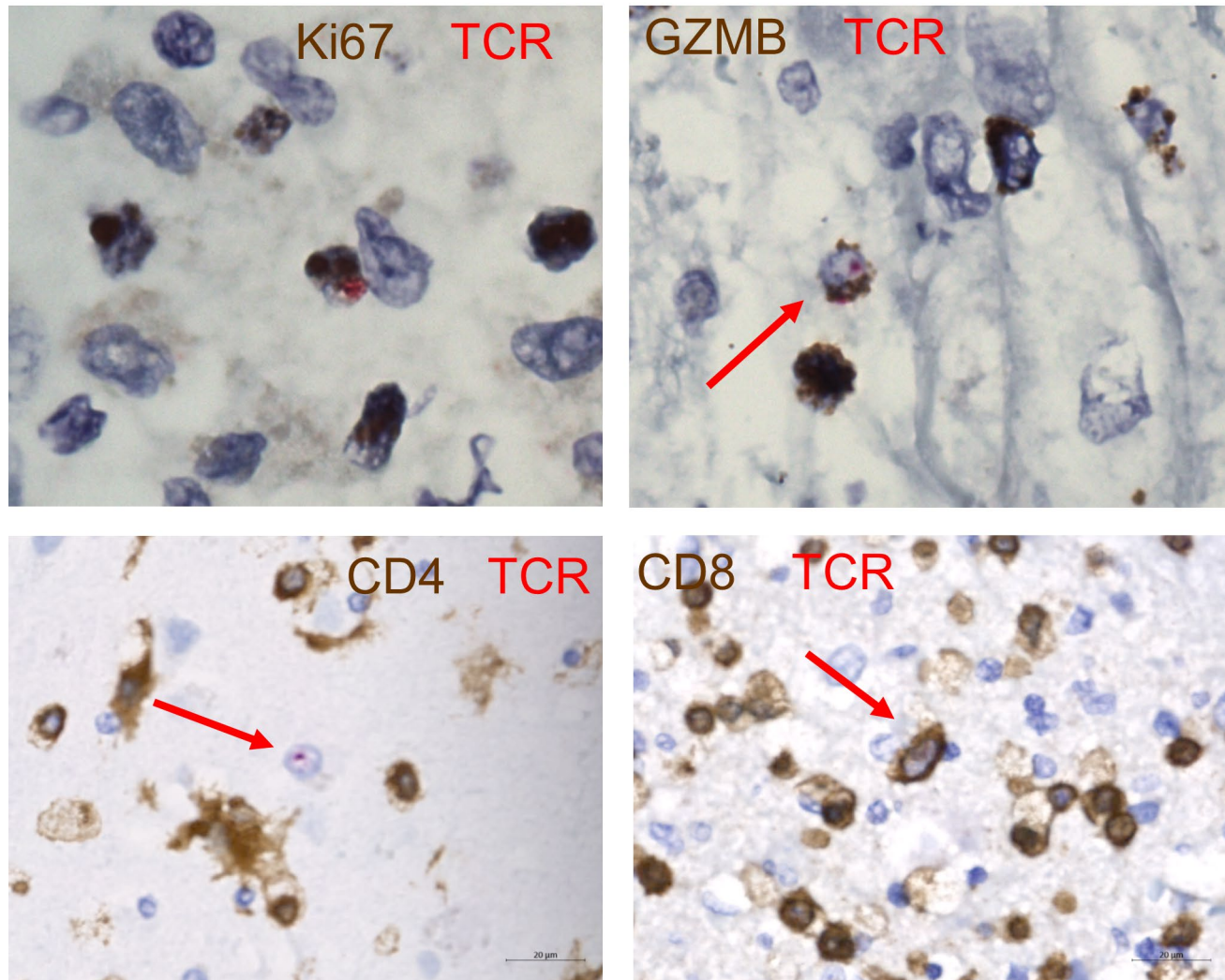
A**B**

Extended Data Fig. 6 | RNA-seq analysis of encephalitic and unaffected tissue. **a**, Absolute and relative quantification of immune subsets by CIBERSORT. **b**, Interferon- γ -inducible genes (HALLMARK_INTERFERON_GAMMA_RESPONSE; M5913; n = counts of 177 overlapping genes per sample) quantified in inflamed and unaffected regions by RNA-seq, as well as additional cases identified in Supplementary Table 3. * adjusted $P < 0.0001$ versus all other samples via analysis of variance (F -statistic = 59.47; $DF_n = 5$; $DF_d = 1,056$) with Tukey's post hoc test to adjust for multiple comparisons; data shown are mean \pm SEM.

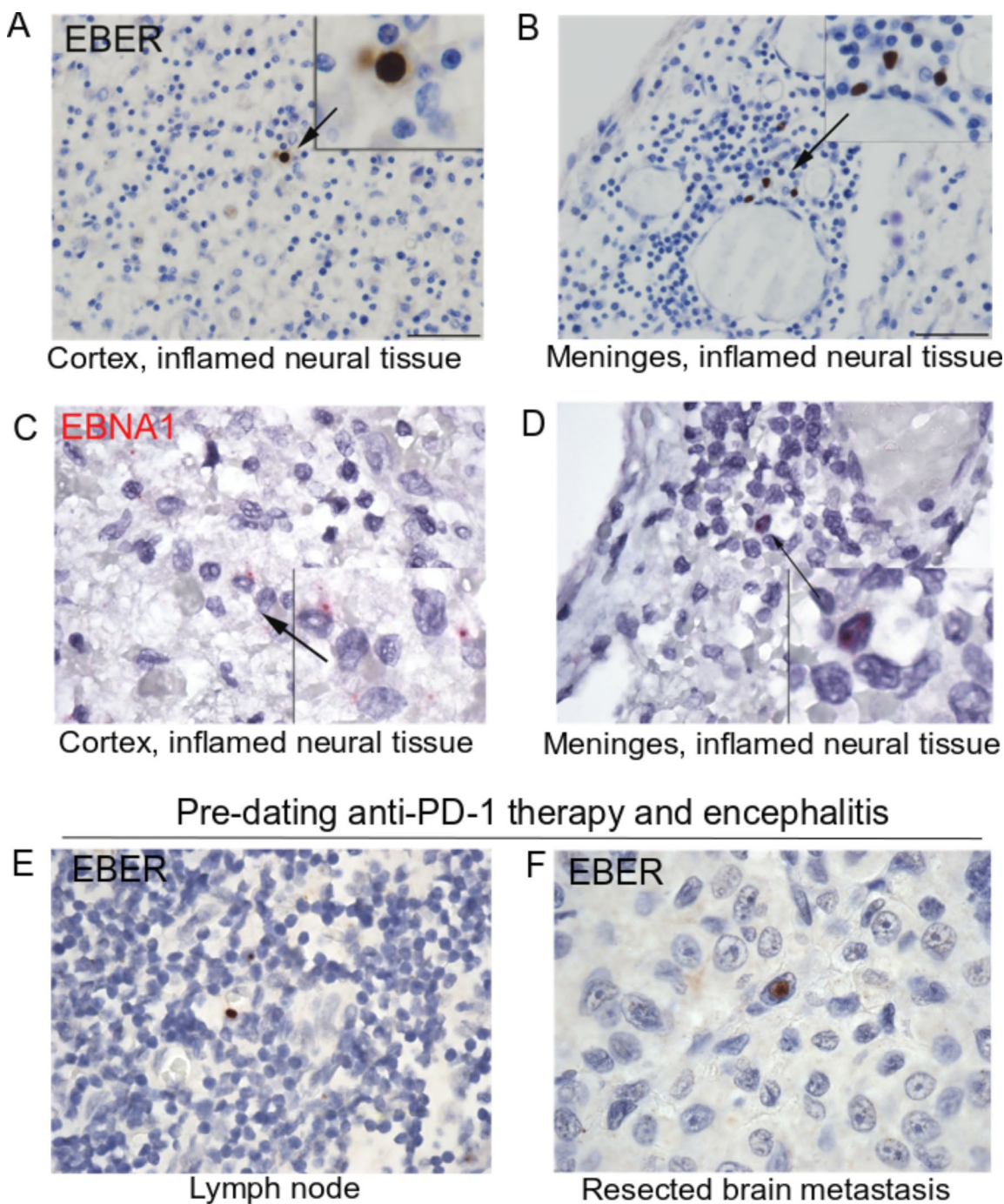


Extended Data Fig. 7 | Analysis of repertoire overlap between inflamed brain and other resected and biopsied tissues. In all panels, we display the frequency of TCRs detected in both the inflamed brain and the listed tissue using the ArcherDX Immunoverse platform, as well as the linear regression and its 95% CIs on a log₁₀ scale. **a**, Lymph node biopsy ($r^2 = 3.19 \times 10^{-8}$; 95% CI of slope, -0.03 to 0.03 ; $F = 8.93 \times 10^{-7}$; $P = 0.99$, $df = 28$). **b**, Prior mesentery resection ($r^2 = 0.04$; 95% CI of slope, -0.09 to 0.02 ; $F = 1.305$; $P = 0.26$, $df = 34$). **c**, Brain recurrence scar—the TCR repertoire of the brain recurrence scar. **d**, Uninflamed brain overlapped significantly with that of the inflamed brain ($r^2 = 0.46$; 95% CI of slope, 0.21 to 0.48 ; $F = 28.19$; $P < 0.0001$, $df = 30$); and ($r^2 = 0.17$; 95% CI of slope, 0.07 to 0.70 ; $F = 6.32$; $P = 0.02$, $df = 31$). EBV-specific clones in both the inflamed brain and the spleen. **e,f**, were observed at high frequency, though the shared TCR repertoires detected in the brain and spleen were poorly correlated (($r^2 = 0.06$; 95% CI of slope, -0.04 to 0.25 ; $F = 2.03$; $P = 0.16$, $df = 32$) and ($r^2 = 5.67 \times 10^{-3}$; 95% CI of slope, -0.20 to 0.32 ; $F = 0.23$; $P = 0.63$, $df = 41$)). **g**, Hierarchical clustering on the F2 distance metric was used to evaluate the similarity of the TCR repertoires from each of the tissue sites sampled from the patient. As also observed above, the brain and spleen samples from 2016 and the time of death were most similar to each other and that the brain-resident TCR repertoire appeared to be somewhat stable over time. The TCR repertoire of the lymph node nearest to the original tumor was highly distinct in comparison with the other samples.

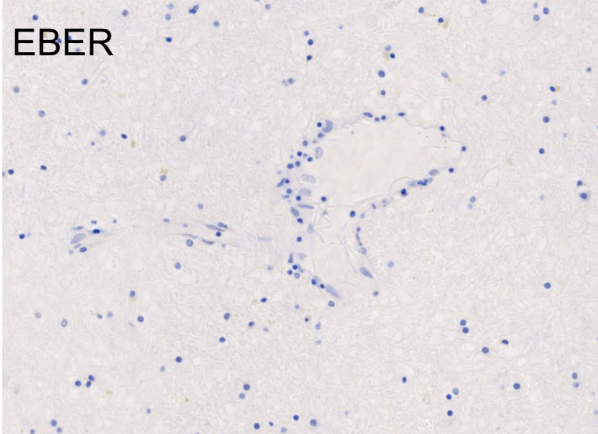
HLA-A*02:01-restricted known EBV-specific TCR
CASSRGQGSADTQYF



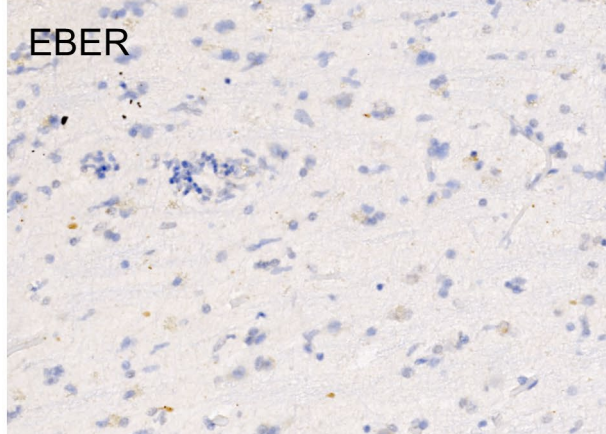
Extended Data Fig. 8 | Overlap of HLA-A*02:01-restricted known EBV-specific TCR with CD8⁺ Ki67⁺ and GZMB⁺ phenotypes. Representative images of the TCR β RNA-ISH probe overlaid with IHC markers. Stains were performed on a single tissue section with a batch-controlled positive and negative control.



Extended Data Fig. 9 | Evidence of latent EBV infection at the site of encephalitic inflammation. **a,b**, EBER(1/2) staining of lymphocytes by RNA in situ hybridization in the cortex and meninges (**a**) and of the encephalitic infarct (**b**). **c,d**, EBNA1 staining of lymphocytes by RNA in situ hybridization in the cortex and meninges (**c**) and of the encephalitic infarct (**d**). **e**, Positive EBER staining of rare lymphocytes in lymph node resection pre-dating anti-PD-1 therapy, suggesting historic EBV infection. **f**, Positive EBER staining of rare tumor cells in brain metastasis resection predating anti-PD-1 therapy, also suggesting historic EBV infection. Stains were performed on a single tissue section with a batch-controlled positive and negative control.

A Additional case 1

EBER

B Additional case 2

EBER

Extended Data Fig. 10 | Lack of detection of EBER⁺ cells in two additional cases of checkpoint inhibitor encephalitis. EBER stain of neural tissue from additional case 1 and additional case 2 (details of case in methods). Stains were performed on a single tissue section with a batch-controlled positive and negative control.

Reporting Summary

Nature Research wishes to improve the reproducibility of the work that we publish. This form provides structure for consistency and transparency in reporting. For further information on Nature Research policies, see [Authors & Referees](#) and the [Editorial Policy Checklist](#).

Statistics

For all statistical analyses, confirm that the following items are present in the figure legend, table legend, main text, or Methods section.

n/a Confirmed

- The exact sample size (n) for each experimental group/condition, given as a discrete number and unit of measurement
- A statement on whether measurements were taken from distinct samples or whether the same sample was measured repeatedly
- The statistical test(s) used AND whether they are one- or two-sided
Only common tests should be described solely by name; describe more complex techniques in the Methods section.
- A description of all covariates tested
- A description of any assumptions or corrections, such as tests of normality and adjustment for multiple comparisons
- A full description of the statistical parameters including central tendency (e.g. means) or other basic estimates (e.g. regression coefficient) AND variation (e.g. standard deviation) or associated estimates of uncertainty (e.g. confidence intervals)
- For null hypothesis testing, the test statistic (e.g. F , t , r) with confidence intervals, effect sizes, degrees of freedom and P value noted
Give P values as exact values whenever suitable.
- For Bayesian analysis, information on the choice of priors and Markov chain Monte Carlo settings
- For hierarchical and complex designs, identification of the appropriate level for tests and full reporting of outcomes
- Estimates of effect sizes (e.g. Cohen's d , Pearson's r), indicating how they were calculated

Our web collection on [statistics for biologists](#) contains articles on many of the points above.

Software and code

Policy information about [availability of computer code](#)

Data collection

The nCounter pipeline was used to collect oligonucleotide count data from the NanoString GeoMX platform. The commercial immuneAnalyzer/immunoSEQ pipeline was used to generate TCR sequencing data from DNA for this study. Proprietary software was used to assign ASHI-accredited 4-digit resolution HLA genotypes as previously described.

Data analysis

VDJTools 1.1.8 was used to process TCR sequencing data and to parse functional TCR sequences. GLIPH version 1 was used for motif enrichment analysis of TCR sequencing data. TCRex version 1 (last accessed 12 October 2018) was used to perform in silico epitope binding predictions with TCR sequencing data. McPAS-TCR and VDJDB were used to annotate TCR sequencing data for known specificities (last accessed 2 June 2019). immunoSEQ data were analyzed with immunoSEQ Analyzer 3.0.

Bcl2fastq2 v.1.8.4 was used to convert raw sequencing data to FASTQ format. QC of RNAseq data was performed using FastQC. STAR 2.2.1 with 2-pass mapping was used to align sequencing reads to GRCh38 (Ensembl, release 85). Further QC after alignment and mapping was performed using RSeQC. Transcripts per million (TPM) were calculated using RSEM. CIBERSORT (cibersort.stanford.edu) was used to characterize the immune cell composition of the RNAseq data. The HALLMARK_INTERFERON_GAMMA_RESPONSE signature from MSigDB was used to score interferon pathway activity.

All statistical testing in R was performed using the base R language, version 3.5.1. GraphPad Prism version 7 was used where listed for other statistical testing.

For manuscripts utilizing custom algorithms or software that are central to the research but not yet described in published literature, software must be made available to editors/reviewers. We strongly encourage code deposition in a community repository (e.g. GitHub). See the Nature Research [guidelines for submitting code & software](#) for further information.

Data

Policy information about [availability of data](#)

All manuscripts must include a [data availability statement](#). This statement should provide the following information, where applicable:

- Accession codes, unique identifiers, or web links for publicly available datasets
- A list of figures that have associated raw data
- A description of any restrictions on data availability

Source data for RNA-seq analyses (IFNy genes) are included as Supplementary Dataset 1. All other data, including processed TCR sequencing data, are available on request from the corresponding authors. The Center for Technology Transfer and Commercialization at Vanderbilt University Medical Center will promptly review all data requests to ensure that intellectual property and confidentiality obligations are met; a Material Transfer Agreement will be used to transfer any and all data that can be shared, including TCR sequencing data.

RNAseq data from this study have been deposited in the database of Genotypes and Phenotypes (https://prod.tbilab.org/balko_lab/encephalitis_NMED/).

Field-specific reporting

Please select the one below that is the best fit for your research. If you are not sure, read the appropriate sections before making your selection.

Life sciences Behavioural & social sciences Ecological, evolutionary & environmental sciences

For a reference copy of the document with all sections, see nature.com/documents/nr-reporting-summary-flat.pdf

Life sciences study design

All studies must disclose on these points even when the disclosure is negative.

Sample size	No sample size calculation was performed. The VigiBase analysis presented in this manuscript is a retrospective analysis utilizing self- and non-self-reported pharmacovigilance data. Experiments utilizing sequencing and imaging technologies were performed on samples from individuals who were consented as part of this study, and appropriate negative controls (such as samples from patients with non-checkpoint inhibitor encephalitis) were selected for analysis to facilitate interpretation.
Data exclusions	No data were excluded from analysis.
Replication	We performed analysis of 2 additional cases of checkpoint inhibitor-associated encephalitis and validated the findings of T lymphocyte infiltration into the affected tissue of brain, in addition to CD68 microglial cell staining. We also assessed other viral etiologies where possible in these cases, and excluded the presence of EBV+ lymphocytes in negative control cases of non-checkpoint inhibitor-associated encephalitis (n=9). Similarly, we validated the significance of PD-L1 expression in the affected tissue of the index case using these same negative control cases.
Randomization	As this is not an intervention-based or clinical study, no randomization was employed.
Blinding	As this is not an intervention-based or clinical study, blinding was not employed.

Reporting for specific materials, systems and methods

We require information from authors about some types of materials, experimental systems and methods used in many studies. Here, indicate whether each material, system or method listed is relevant to your study. If you are not sure if a list item applies to your research, read the appropriate section before selecting a response.

Materials & experimental systems

n/a	Involved in the study
<input type="checkbox"/>	<input checked="" type="checkbox"/> Antibodies
<input checked="" type="checkbox"/>	<input type="checkbox"/> Eukaryotic cell lines
<input checked="" type="checkbox"/>	<input type="checkbox"/> Palaeontology
<input checked="" type="checkbox"/>	<input type="checkbox"/> Animals and other organisms
<input type="checkbox"/>	<input checked="" type="checkbox"/> Human research participants
<input checked="" type="checkbox"/>	<input type="checkbox"/> Clinical data

Methods

n/a	Involved in the study
<input checked="" type="checkbox"/>	<input type="checkbox"/> ChIP-seq
<input checked="" type="checkbox"/>	<input type="checkbox"/> Flow cytometry
<input checked="" type="checkbox"/>	<input type="checkbox"/> MRI-based neuroimaging

Antibodies

Antibodies used

Anti-CD45RO (Thermo Scientific, cat# MA5-11532; clone UHCL1), validated reactivity in humans and not mouse, rat, or non-human primate, validated with data available by manufacturer for western blot, IHC, and FACS. Anti-GZMB (Biocare cat# ACI 3202 AA, prediluted, clone 11F1), validated reactivity against human GZMB in spleen and tonsillar tissue, validated lack of reactivity in 27 healthy human tissues and 8 cancerous human tissues (positive control peripheral T cell lymphoma). Anti-Ki67, (Dako, cat# M7240, 1:200 dilution, clone MIB-1), validated reactivity against IM-9 cell line with 345 and 395 kDa bands as labelled by original anti-Ki67 via western blot, competitive binding, and identical staining patterns via IHC on serial tonsillar frozen sections. Anti-CD4 (StatLab, cat#RM27-10, prediluted) and anti-CD8 (StatLab, cat#MM39-10, prediluted, clone 144B),

validated by stain of cytotoxic/suppressor T cells, staining pattern similar to clustered CD8 monoclonal antibodies, reacts specifically with a 32 kDa band via western blot. Anti-PD-L1 (ThermoFisher cat# PA5-28115, 1:7500, polyclonal), validated via IHC and western blot after shRNA knockdown of PD-L1 and in A549 cell extracts and membrane extracts. Anti-CD68 (abcam cat# ab125212, 1:600, polyclonal), validated by staining of tonsillar and bowel tissue macrophages, negative staining of 201 human tumors, positive staining of myelomonocytic lineage cells in 47 normal case tissues and negative staining of endothelial cells. Anti-PD-1 (Sigma-Aldrich cat# HPA035981, 1:75, polyclonal), validated staining of lymph node and liver, confirmed specificity via western blot. Anti-CD20 (Leica Biosystems cat# PA0906, prediluted, clone L26), validated by tonsillar staining, negative staining of cerebellum, positive staining of B cells in 96 healthy human tissue cases and B cell lymphomas, negative staining of T and NK/T lymphomas and multiple other tumor types. CD244 (Proteintech, Catalog# 16677-1- AP, dilution 1:200, polyclonal), CD160 (Abcam, cat# ab202845, dilution 1:600, polyclonal) and Lag3 (CST, cat#15372, 1:200 clone D2G4O) were validated in healthy human tonsil (positive staining of immune cells), human healthy brain (negative for background). Anti-fluorescein (Leica, cat# AR0833, no dilution required, clone ID not available) is a purified IgG fraction of a mouse monoclonal antibody at a concentration of 0.108 ug/mL.

Validation

In addition to validation data described above, all antibodies used in this paper have been used in previous studies by other research groups.

Human research participants

Policy information about [studies involving human research participants](#)

Population characteristics

Age and gender of all study participants are provided in the main Tables. Negative control cases (n=9) consisted of both men (n=5) and women (n=4), with younger ages (Rasmussen's encephalitis, 3 and 5 years old) and older ages (25,34,40,50,50,62,63). Study participants were recruited based on their clinical presentation and histories (cancer, non-cancer) and encephalitic etiology (infectious, non-infectious, checkpoint inhibitor associated).

Recruitment

Participants were recruited under IRB-approved protocols and selected for recruitment by physicians based on their medical histories and presentation (encephalitis associated with or without checkpoint inhibitor therapy). No formal recruitment was performed other than approaching all new patients for prospective biospecimen banking for research purposes.

Ethics oversight

The IRB of Vanderbilt University Medical Center approved the study protocol as noted in further detail in the manuscript.

Note that full information on the approval of the study protocol must also be provided in the manuscript.